Check for updates

steel research international
www.steel-research.de

Recycling End-of-Life Solid Oxide Cell Interconnect Assemblies into Commercial-Grade AISI 304 Stainless Steels

Jeraldine Lastam, Shine-Od Mongoljiibuu, Alexander Specht, Daniel Grüner, Dmitry Sergeev, Urs A. Peuker, Michael Müller, and Ruth Schwaiger*

To support the sustainable industrialization of solid oxide cell (SOC) stacks, the present study proposes and experimentally validates a recycling pathway to recover interconnect assemblies from end-of-life Jülich SOC stacks. The recycling process utilizes scrap-based steelmaking operations to produce steels with comparable chemical composition, microstructure, and hardness to commercial-grade AISI 304 steels. Results from smelting demonstrate a high metal yield of 95.7% and controlled deportation of metallic resources into the slag phase. X-ray computed tomography analysis of the slag shows metal inclusions with sizes less than 1.7 mm and accounting for ≈2.01 vol% of the slag. Furthermore, the slag contains a relatively high amount of chromium (3.61 wt% Cr), and minor amounts of iron (1.02 wt% Fe) and manganese (0.90 wt% Mn). Subsequent refinement and heat treatment of the smelted alloy have successfully produced austenitic steel with less than 4.0% δ-ferrite area fraction. Microindentation tests confirm that its hardness values are consistent with the typical values for AISI 304 steels. Furthermore, high-temperature X-ray diffraction analyses provide valuable insights into the recycled steel's relative austenite stability regions. Finally, potential challenges and opportunities associated with scaling up the proposed recycling route are discussed.

1. Introduction

The role of global hydrogen deployment toward achieving net-zero emissions has gained traction in recent years.[1] Climate agencies such as the International Renewable Energy Agency (IRENA) and the International Energy Agency (IEA) have outlined ambitious 2050 decarbonization scenarios, setting the global electrolysis capacity targets at 4.4 TW and 3.3 TW, respectively.[1,2] As of 2023, 24 countries have announced their green H_2 initiatives, including Germany, which aims to reach 10 GW of installed electrolyzers by 2030 through its H_2Giga national project.[3,4] In anticipation of the massive surge in new technological wastes, the ReNaRe subproject has been launched to develop recycling solutions for prospective end-of-life electrolysis and fuel cell stacks.[5]

Solid oxide cells (SOCs) are potential candidates for scale-up, attributed to their high electrical efficiencies and capacity for waste heat recovery among other reasons.[6] Forschungszentrum Jülich (Jülich) has over 30 years' experience in SOC stack testing and development, with fuel electrode-supported "F-design" stacks as its main design for stationary applications.[7,8] These stacks, generally classified as F10 or F20 depending on total cell dimensions per layer (F10: $10 \times 10\,cm^2$ cell; F20: $20 \times 20\,cm^2$ cell), can achieve increased electrical capacities by stacking together repeating units of cell and interconnect assemblies,[8] as depicted in **Figure 1**a.

Recent studies have increasingly focused on ceramic cell recycling in SOC stacks.[9–13] However, similar research related to metallic parts remains limited. Nevertheless, prioritizing the recycling and reuse strategies for these materials is of critical importance, as they constitute the majority of the stack's weight and cost. A manufacturing model for anode-supported cell (ASC)-based 5 kW_{el} Jülich F20 stacks by Harboe et al.[14] shows that the material costs are roughly three to four times higher than the combined costs for labor, energy, and machining at 25 MW_{el} annual stack production. Furthermore, the metallic components dominate the material costs and exceed those of the cells by a factor of 17 (Figure 1b). This is mainly attributed to their substantial contribution to the total stack weight, with interconnect assemblies, i.e., interconnector and nickel meshes, accounting for ≈70 wt% of the stack (Figure 1c). Although similar data from

J. Lastam, D. Grüner, D. Sergeev, M. Müller, R. Schwaiger
Structure and Function of Materials (IMD-1)
Institute of Energy Materials and Devices (IMD)
Forschungszentrum Jülich GmbH
Wilhelm-Johnen Strasse, 52425 Jülich, Germany
E-mail: j.lastam@fz-juelich.de

S.-O. Mongoljiibuu, U. A. Peuker
Institute for Mechanical Process Engineering and Mineral Processing (MVTAT)
Technische Universität Bergakademie Freiberg
Agricolastrasse 1, 09599 Freiberg, Germany

A. Specht
Institute of Process Metallurgy and Metal Recycling (IME)
RWTH Aachen University
Inzestrasse 3, 52072 Aachen, Germany

D. Sergeev
NETZSCH Analyzing and Testing
NETZSCH-Gerätebau GmbH
Wittelsbacherstrasse 42, 95100 Selb, Germany

The ORCID identification number(s) for the author(s) of this article can be found under https://doi.org/10.1002/srin.202500384.

© 2025 The Author(s). Steel Research International published by Wiley-VCH GmbH. This is an open access article under the terms of the Creative Commons Attribution License, which permits use, distribution and reproduction in any medium, provided the original work is properly cited.

DOI: 10.1002/srin.202500384

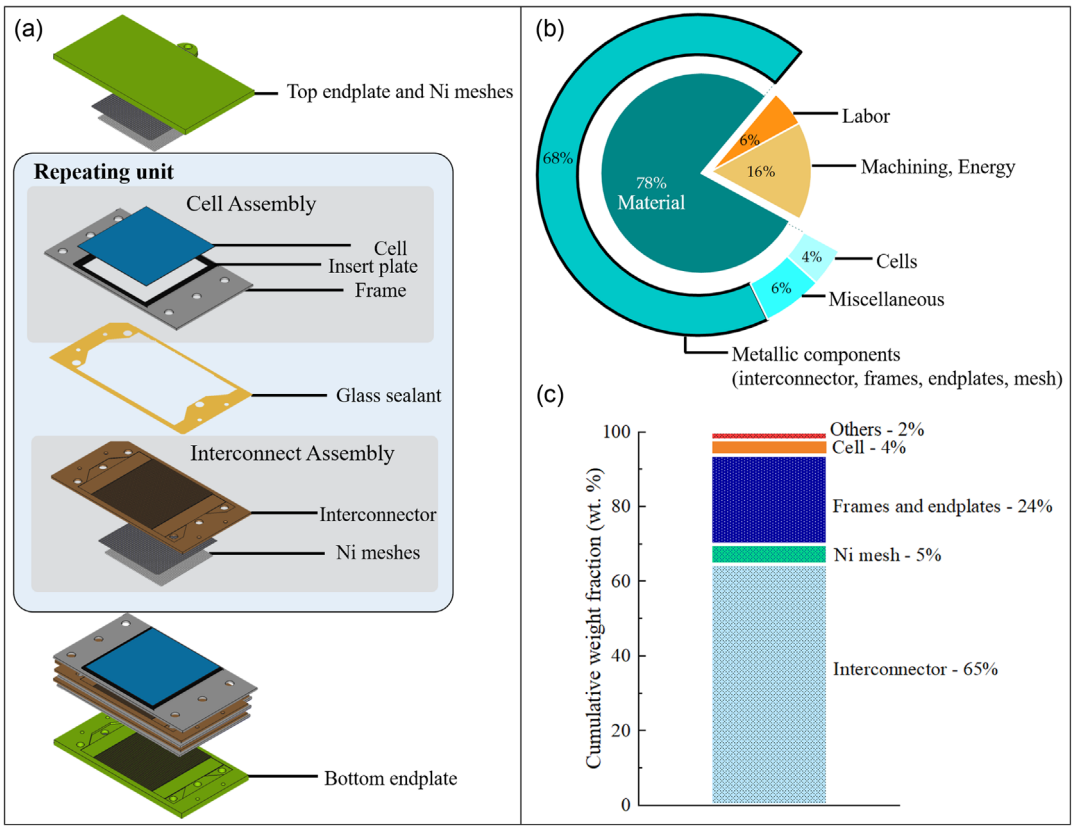

Figure 1. a) Schematic illustration of Jülich F stack, b) estimated breakdown of direct production costs for Jülich F20 stack at 25 Mw_{el} $year^{-1}$ production volume, and c) the weight fractions of various components (wt%) in a 5 kW_{el} Jülich F20 stack.[14]

other SOC stack manufacturers are limited, Hwang et al.[15] reported a comparable value of 76 wt% in ASC-based SOC stacks using life cycle inventory calculations. Developing a viable recycling pathway for interconnect assemblies is, therefore, crucial to sustainable SOC stack production.

Steel scraps are conventionally recycled via remelting[16] while highly contaminated metal waste streams, such as electronic wastes and EV batteries, are processed using more complex pyro- and hydrometallurgical methods.[17,18] Since SOC interconnect assemblies are steel-based materials with adhered layers in the form of meshes and coatings, existing literature generally recommends their bulk remelting into alternative steels.[19–21] However, detailed studies on this route remain limited.

Steel is an indispensable commodity in the modern world and is expected to remain in high demand for the foreseeable future.[22] Often regarded as a "wonder alloy" for its versatility and affordability, one of steel's most important features is its high potential for recycling.[23] Steel is conventionally produced through the integrated blast furnace-basic oxygen furnace (BF-BOF) route, which mixes around 15–20 wt% of steel scraps with primary iron.[23,24] It currently accounts for ≈71.1% of the global steel production, while scrap-based electric arc furnace (EAF) steelmaking holds only about 28.6% of the market share.[22] The challenge with the BF-BOF route is, however, evident—it utilizes significant amounts of metallurgical coke and thus releases substantial amounts of CO_2.[25] For this reason, steel production is currently the largest carbon emitter among all metal industries and is responsible for about 7–9% of global greenhouse gas emissions.[24,25]

Although highly electricity-dependent, the scrap-based EAF route emits roughly three times less CO_2 than the BF-BOF route, making it an attractive pathway toward decarbonization in the steel sector.[22,24] A study by Harpprecht et al.[24] predicts that with the availability of clean electricity from renewable energies and green hydrogen, scrap-based EAF steels could supply over 50% of global steel demand by 2050, with the rest coming from hydrogen-based direct iron reduction and iron ore electrowinning.

The global demand for stainless steel has been steadily rising, reaching ≈58.4 million metric tonnes in 2023.[26] CrNi-based stainless steels dominate this market and account for roughly 60% of the total melt shop production,[27] with AISI 304 steels, or commonly known as "18/8", as being one of the most widely used grades.[28] Therefore, developing a route to recycle other sources of materials into stainless steel would be a boon in terms of cost reductions and emissions. To this end, our previous study[19] identified Jülich F stack interconnect assemblies as potential secondary sources for AISI 304 steels. Utilizing these scraps as 100% feedstock for steel production promotes material circularity, and therefore, contributes to decarbonization in both the steel and energy sectors. However, the previous research was limited to small-scale specimens extracted from the interconnect

© 2025 The Author(s). Steel Research International published by Wiley-VCH GmbH

1869344x, 0, Downloaded from https://onlinelibrary.wiley.com/doi/10.1002/srin.202500384 by Rwth Aachen University Zentraler Rechnungseingang, Wiley Online Library on [22/07/2025]. See the Terms and Conditions (https://onlinelibrary.wiley.com/terms-and-conditions) on Wiley Online Library for rules of use; OA articles are governed by the applicable Creative Commons License

assembly, while larger-scale steelmaking has not yet been performed.

Scrap-based AISI 304 steel production is, however, not a simple matter of melting metallic waste; it requires precise control of metallurgical and processing parameters to achieve the desired compositional, microstructural, and mechanical properties. This begins with smelting, commonly carried out in an EAF where scraps are melted in the presence of oxide fluxes to yield a bulk alloy and protective slag.[16,29] In smelting operation, the right slag composition must be ensured for effective collection of impurities by the slag without compromising the metal yield.[29] This is particularly challenging with stainless steel melts, where high chromium levels (16–26 wt%) need to be maintained despite chromium's strong affinity for oxygen.[30] Many authors report that low chromium solubilities in the slag can be achieved by using slightly basic, spinel-saturated slags with basicity ratios ranging between 1.2 and 1.7.[29,31,32]

A common approach for predicting the steel's microstructure based on composition involves calculating its chromium equivalent (Cr_{eq}) and nickel equivalent (Ni_{eq}) values.[33–35] These parameters quantify the contributions of ferrite and austenite stabilizing elements to the phase balance in as-casted alloys and are determined from the chemical compositions (wt%) using the following equations.[34]

$$Cr_{eq} = Cr + Mo + 4Ti + 4Al + 1.5Si + 1.5V + 0.9Nb + 0.9Ta + 0.5W \quad (1)$$

$$Ni_{eq} = Ni + 30C + 18N + 0.5Mn + 0.3Co + 0.2Cu - 0.2Al \quad (2)$$

In lean austenitic steels such as AISI 304, austenite is thermodynamically metastable and may transform to martensite when cooled down below its martensite start temperature (M_s).[36,37] This instability can be influenced by the balance between the Ni_{eq} and Cr_{eq} values. For instance, Weiss et al.[34] reported that a cast austenitic stainless steel exhibiting transformation-induced plasticity (TRIP) effect exhibited Ni_{eq} values between 8 and 16, and Cr_{eq} values between 14 and 22. To ensure phase stability, compositional fine-tuning is typically carried out through refinement, either within the EAF or in a secondary furnace equipped for impurity removal, degassing, and alloying.[16,29] The casts then undergo heat treatment such as solution annealing at 1010–1175 °C to dissolve detrimental intermetallic phases and minimize elemental segregation.[38]

The present study, therefore, evaluates the feasibility of transforming a Jülich F stack interconnect assembly into AISI 304 steel through conventional scrap-based steelmaking operations. Additionally, this research aims to bridge the gap between laboratory-scale and industrial-scale steelmaking processes, identify potential issues, and gain a deeper technical understanding associated with scaling up.

The composition, microstructure, mechanical, and thermophysical properties of the product steels were compared with those of commercial AISI 304 steels. Specifically, electron backscatter diffraction (EBSD) and energy-dispersive X-ray spectroscopy (EDX) techniques were utilized to quantify the microstructural constituents in recycled steels. Microindentation testing was employed to assess the Vickers hardness (HV) values, while high-temperature X-ray diffraction (HT-XRD) was performed to determine the relative M_s values of the studied alloys.

2. Experimental Section

An interconnect assembly constituted of an interconnector and three Ni meshes (Ni mesh 1: $2.0 \times 0.6\ mm^2$; Ni mesh 2: $0.2 \times 0.125\ mm^2$; and Ni mesh 3: $1.3 \times 0.3\ mm^2$) was utilized in this study. The interconnector was comprised of a Crofer 22 APU steel substrate coated on the air-side with $MnCo_{1.9}Fe_{0.1}O_4$ (MCF) and $LaMn_{0.45}Co_{0.35}Cu_{0.2}O_3$ (LCC10), while Ni meshes were soldered on its fuel-side. Traces of the Type 87 ZYBF-2 glass sealant were also present at contact areas with adjacent layers. The interconnect assembly was obtained from a four-layer Jülich SOC F10 stack (F1004-94), which had previously operated for 2700 h at 800 °C in coelectrolysis mode. Further details on the stack's operating history can be found elsewhere.[39] The schematic and photographic images of the interconnect assembly are shown in **Figure 2**.

The interconnect assembly was placed inside an yttrium-stabilized zirconia crucible and covered with a basic oxide flux composed of CaO/SiO_2 (1.7 w w^{-1}, 20 wt% to the total feed). The CaO was produced by thermally decomposing $CaCO_3$ (Rheinkalk, Wülfrath, Germany, 94.6%) at 650–680 °C for 6 h, while commercially available amorphous SiO2 powders (Sibelco, Dessel, Belgium, 99%) were used. The feed was then heated inside a high-temperature furnace to 1550 °C at 10 °C min^{-1} and held for ≈7 h under argon gas at 15 L min^{-1} to ensure complete melting. Subsequent casting was performed in a graphite-coated cast iron mold. The smelting metal yield, correlated to the recovery rate of metallic elements, was calculated as follows.

$$\text{Metal Yield}\ (\%) = \frac{\text{Mass of output alloy}\ (g)}{\text{Mass of interconnect assembly}\ (g)} \times 100\% \quad (3)$$

The air-quenched slag was collected and analyzed with X-ray computed tomography (XCT) to assess its phase homogeneity. XCT is a nondestructive imaging technique that provides a 3D visualization of internal structures, identifying potential heterogeneities or inclusions that could influence subsequent analyses. For the XCT analysis, slag samples were fixed with sugar as a spacer material in a plastic sample holder (3 mm diameter) and scanned using a Zeiss Xradia 510 Versa X-ray microscope (Carl Zeiss AG, Oberkochen, Germany). The slag fragments were scanned with two sets of parameters: (a) in a large field of view (140 keV, 10 W, 20.3 µm voxel size) to get an overview of the whole sample and (b) in a smaller field of view (130 keV. 10 W, 9.8 µm voxel size) to get a higher resolution and more detailed information on the phases. After scanning, the reconstruction (Scout & Scan Reconstructer, v 16.1.13 038) and preprocessing (Fiji, v 1.54f) of images were performed.

Following the XCT analysis, the metallic inclusions were removed using magnetic separation and sieving. The slag sample was then split into four subsamples by cone and quartering. Two of these subsamples were homogenized and ground to a fine powder (<63 µm) for bulk analyses, while the remaining

© 2025 The Author(s). Steel Research International published by Wiley-VCH GmbH

1869344x, 0, Downloaded from https://onlinelibrary.wiley.com/doi/10.1002/srin.202500384 by Rwth Aachen University Zentraler Rechnungseingang, Wiley Online Library on [22/07/2025]. See the Terms and Conditions (https://onlinelibrary.wiley.com/terms-and-conditions) on Wiley Online Library for rules of use; OA articles are governed by the applicable Creative Commons License

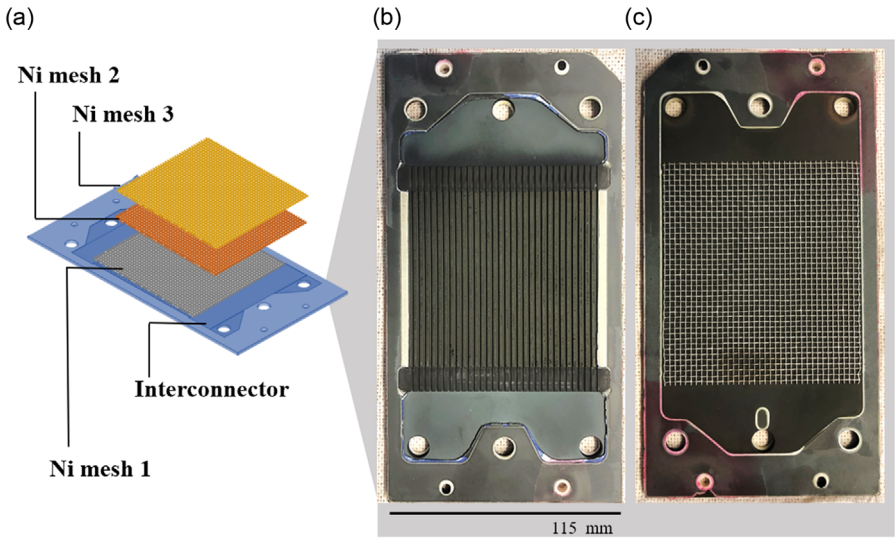

Figure 2. Illustration of a) the interconnect assembly used in this study; photographic images of the interconnector and Ni mesh 1 from the b) air and c) fuel sides, respectively.

subsamples were used for microstructural analysis. A one-gram ground sample was analyzed using wavelength dispersive X-ray fluorescence (WD-XRF) spectroscopy (PANalytical Axios spectrometer, Malvern Panalytical, Kassel, Germany) to quantify major oxides, such as SiO_2, CaO, Al_2O_3, MgO, and Fe_2O_3, as well as elements such as nickel, chromium, and manganese. This analysis was used to assess the metal deportation into slag. Unmilled slag fragments were embedded in a low-viscosity epoxy resin and polished for analysis using a scanning electron microscope (SEM) with EDX. The microstructure of phases, metal-rich regions, and their interaction with the slag matrix were observed via SEM XL30 (Philips, Netherlands).

Refinement trials were performed by extracting specimens (≈30 g) from the base alloy and melting together with nickel mesh (TEDRA-Dahmen, Wassenberg, Germany, 99.0%, 550 mg) and manganese chips (Sigma-Aldrich, Taufkirchen, Germany, 99.0%, 600 mg) in a vertical tube furnace at 1550 °C for 1 h under argon gas at 800 mL min^{-1}. The heating and cooling rates were both 10 °C min^{-1}, respectively. The base and refined alloys were then solution-annealed inside a high-temperature chamber furnace at 1050 °C for 1 h under atmospheric air, followed by water quenching.

For determining the chemical compositions, the bulk alloy was sectioned into halves, and specimens (250 to 300 mg) were extracted from the left, central, and right regions of the halved alloy. The specimens were then analyzed with an inductively coupled plasma-optical emission spectroscopy technique (ICP-OES, iCAP 7600, Thermo Fisher Scientific, Massachusetts, USA). Another set of specimens with dimensions $10 \times 10 \times 5\ mm^3$ was embedded in epoxy resin, ground, and polished under SiO_2 suspension. Their microstructures were subsequently analyzed with a SEM (MERLIN, Zeiss, Oberkochen, Germany) equipped with both an EBSD detector and EDX spectrometer (NordlysNano EBSD and Ultim 100 EDX, Oxford Instruments, High Wycombe, UK). The HV values were determined through microindentation testing (Fischer HC 100, Helmut Fischer KG, Sindelfingen, Germany) of the same polished specimens under argon gas. During microindentation, cyclic loading was applied by increasing the load from 0 to 1000 mN across 20 steps for 120 s. Six to eight indentations were employed for each sample.

The relative M_s values of the alloys were determined using the HT-XRD technique on a final set of extracted specimens ($10 \times 5 \times 3\ mm^3$). The measurements were performed using an EMPYREAN Diffractometer (Malvern Panalytical B. V., Almelo, The Netherlands) equipped with an oven chamber HTK 1200 N (Anton Paar, Graz, Austria) under high vacuum conditions ($p < 1 \times 10^{-4}$ mbar). During HT-XRD experiments, the alloys were initially homogenized at 950 °C for 1 h to ensure full austenitization. They were subsequently scanned at a continuous cooling rate of 2 °C min^{-1} until room temperature was reached. Static 1D scans at 1.5 scans min^{-1} were performed within the range of 41.83°–45.17° 2θ, wherein the strongest face-centered cubic (FCC) and body-centered cubic (BCC) reflections corresponding to the main steel phases can be found.[40]

3. Results and Discussion

3.1. Smelting

3.1.1. Bulk Alloy Composition and Yield

A high metal yield of 95.7% was successfully achieved after smelting, as shown in **Table 1**. The unaccounted output material of around 34 g was likely due to slag penetration into the crucible. Additionally, the bulk alloy demonstrated high compositional homogeneity based on the elemental compositions of specimens extracted from zones 1, 2, and 3 within the alloy, indicative of effective melt mixing (**Figure 3** and **Table 2**). Compared to the predicted composition of the interconnect assembly from a similar stack design investigated in our previous work,[19] this bulk alloy contained lower concentrations of chromium, nickel, cobalt,

© 2025 The Author(s). Steel Research International published by Wiley-VCH GmbH

1869344x, 0, Downloaded from https://onlinelibrary.wiley.com/doi/10.1002/srin.202500384 by Rwth Aachen University Zentraler Rechnungseingang, Wiley Online Library on [22/07/2025]. See the Terms and Conditions (https://onlinelibrary.wiley.com/terms-and-conditions) on Wiley Online Library for rules of use; OA articles are governed by the applicable Creative Commons License

Table 1. Smelting input and output weights, and corresponding metal yield.

Input weight [g]		Output weight [g]			Metal Yield [%]
Interconnect	Flux	Metal	Slag	Unaccounted	
412.52	107.23	394.70	91.30	33.75	95.7

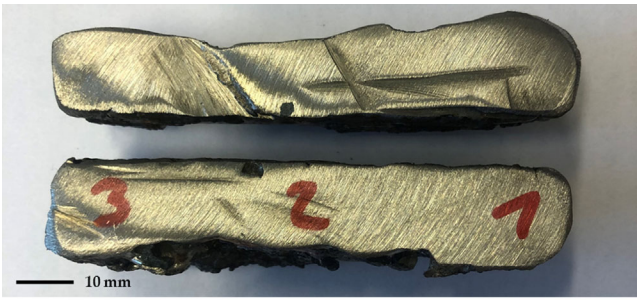

Figure 3. Bulk alloy with marked zones from which specimens were extracted for ICP-OES elemental analysis.

and manganese. In particular, Cr content was ≈2.2 wt% lower, which may be attributed to increased chromium partitioning into the slag under upscaled smelting conditions. However, differences in other elements were minimal, and the overall composition could be considered consistent with predicted values.

3.1.2. Slag Characterization

The phase homogeneity of the slag was assessed using XCT, and the results are presented in **Figure 4**. Figure 4a–c shows the single slices from image stacks of the slag samples for different particle size fractions (1–4, 4–6.3, and 6.3–10 mm). Regions with high absorption, such as the metallic inclusion, are indicated as bright phases in the images, while pores are denoted by dark regions. The grayscale of the images represents the X-ray attenuation, which is a function of several variables such as the material's atomic number, the wavelength of the X-ray, the material thickness, and the material density.[41] The slag appeared largely uniform with a significant presence of metallic inclusions distributed throughout the slag matrix. Different metallic inclusions were observed: Ni inclusion as the brightest phase (Me) and Crofer alloy as the second brightest phase (Me II) are shown in Figure 4a–c. It is important to note that the compositions of these metallic inclusions were later confirmed by SEM-EDX. The observed differences in homogeneity between the bulk slag and individual metallic droplets likely resulted from phase separation during cooling. While the slag appears macroscopically homogeneous, localized variations can arise due to the immiscibility of certain metal phases, differences in melting points, and oxidation states.[42] These factors can lead to the segregation of small metallic droplets with compositions distinct from the bulk slag.

Metal inclusions within the slag samples are indicated by blue regions in the 3D reconstruction images in Figure 4d–f. These inclusions were further analyzed to estimate their sizes and percentage to the total slag volume. The analysis identified inclusions up to 1.7 mm in equivalent spherical diameter, with a characteristic particle diameter of the total inclusion accounting for ≈2.01 vol% of the total scanned volume across all three samples. Most of the inclusions (80% passing) were smaller than 100 µm by number according to the results from particle size analysis (see Figure S1, Supporting Information).

The chemical composition of the slag is summarized in **Table 3**. The result showed the highest concentration of Cr, followed by Fe and Mn, with slight Ni deportation likely originating from the Ni mesh. Traces of Ti, Ba, and Al from the glass sealant were also detected in the slag. Furthermore, the presence of CaO and SiO_2 was attributed to the fluxes, while ZrO_2 was identified to be originating from the crucible material.

SEM-backscatter electrons (SEM-BSE) images revealed the presence of silicates containing minor amounts of Cr, Zr, and Fe, along with spinels, mainly chromite (Cr_2FeO_4), embedded within the slag matrix (**Figure 5**). Additionally, the spinels observed in Figure 5b appeared as intergrown crystals with very fine grains, likely due to the rapid cooling process. Furthermore, metallic inclusions were observed either as Ni droplets or with a composition comparable to that of the base FeCr alloy. The elemental mapping in **Figure 6** shows the deposition of Cr into the chromite spinel, with Cr mainly concentrated in one phase. This finding is consistent with the results of our previous work[19] that employed the same flux composition.

3.2. Refinement and Heat Treatment

The elemental composition of the smelted alloy "S" was within the typical compositional range for AISI 304 steels, except for its Ni content, which was lower by roughly 0.3 wt% (**Table 4**). In addition, the smelted alloy yielded a marginally low Ni_{eq} value (8.68). To increase this value, the alloy composition was adjusted through manganese and nickel additions, which resulted in three

Table 2. Zonal and average elemental compositions (in wt%). The interconnect assembly composition from the previous work is included for comparison.

Zone	Fe	Cr	Ni	Co	Mn	La
1	73 ± 2	18.4 ± 0.7	7.6 ± 0.4	0.47 ± 0.02	0.239 ± 0.004	<0.003
2	73 ± 3	18.5 ± 0.6	7.6 ± 0.4	0.46 ± 0.01	0.240 ± 0.005	<0.003
3	73 ± 4	18.7 ± 0.5	7.9 ± 0.3	0.47 ± 0.02	0.248 ± 0.008	<0.003
Average	73 ± 3	18.5 ± 0.6	7.7 ± 0.4	0.47 ± 0.02	0.242 ± 0.010	<0.003
Previous work[19]	68.9	20.7	8.2	0.9	1.0	–

© 2025 The Author(s). Steel Research International published by Wiley-VCH GmbH

1869344x, 0, Downloaded from https://onlinelibrary.wiley.com/doi/10.1002/srin.202500384 by Rwth Aachen University Zentraler Rechnungseingang, Wiley Online Library on [22/07/2025]. See the Terms and Conditions (https://onlinelibrary.wiley.com/terms-and-conditions) on Wiley Online Library for rules of use; OA articles are governed by the applicable Creative Commons License

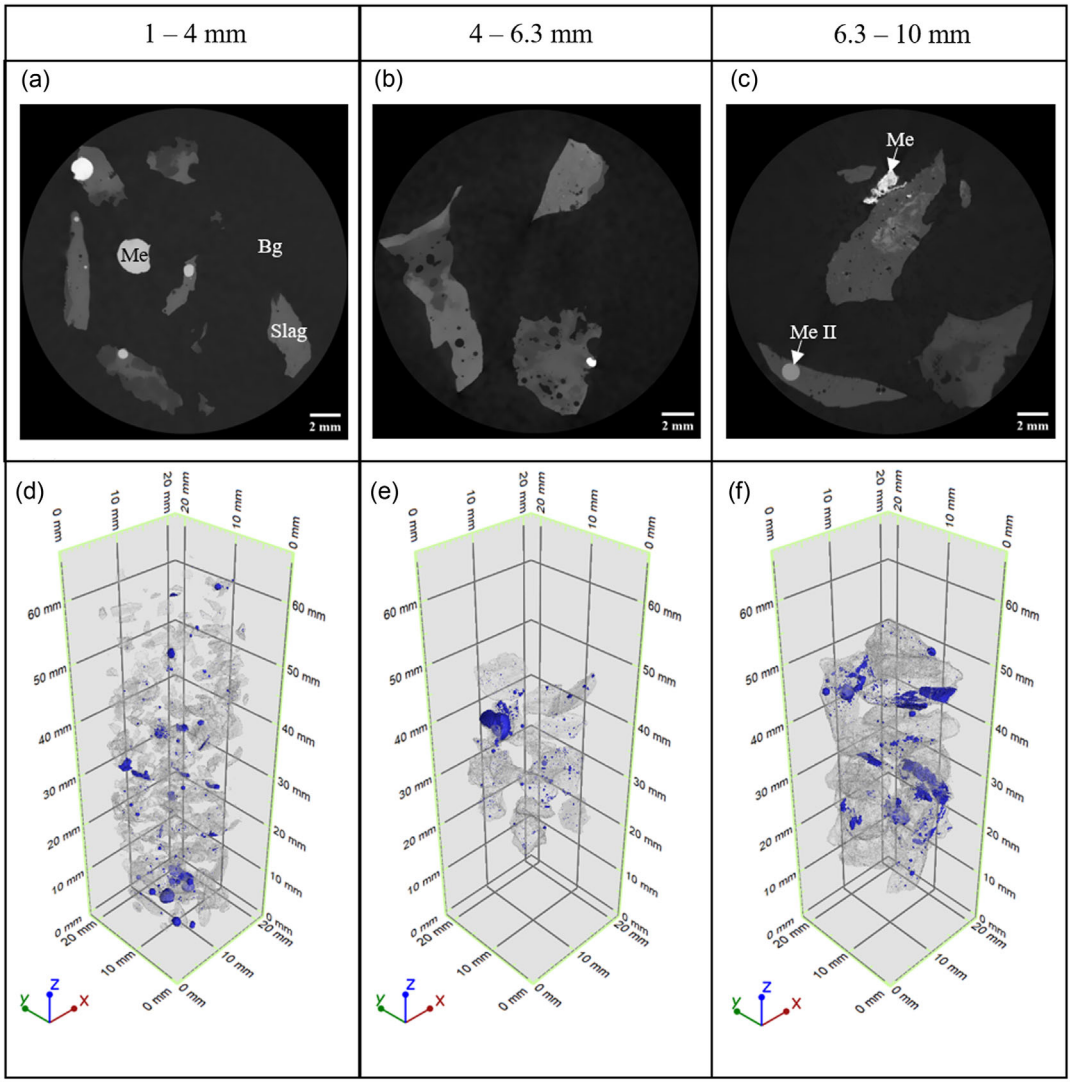

Figure 4. Single-slice images after reconstruction and preprocessing (Me, Me II: metal inclusions; Bg: background) and 3D renderings of reconstructed slags with the following particle size fractions: a,d) 1–4 mm, b,e) 4–6.3 mm, and c,f) 6.3–10 mm, respectively. Metallic inclusions are highlighted as bright phases in the single-slice images and as blue regions in the 3D reconstruction images.

Table 3. Chemical composition (wt%) expressed in oxide forms of the quenched slag determined by WDXRF. Loss on ignition (LOI) is included for information.

Sample	LOI	CaO	SiO_2	Al_2O_3	MgO	Fe_2O_3	MnO	Cr_2O_3	TiO_2	ZrO_2	BaO	NiO
Slag	0.14	49.82	32.38	0.58	0.53	1.49	1.16	5.28	0.24	5.60	1.33	0.51

refined alloys: one containing ≈2 wt% Mn, another containing 9 wt% Ni, and a third one with both 9 wt% Ni and 2 wt% Mn. Their elemental compositions were obtained from ICP-OES elemental analysis and summarized in Table 4. Following refinement, the alloys were solution-annealed at ≈1050 °C for 1 h and then water-quenched. For ease of reading, the investigated alloys were designated as follows: S for smelted unrefined alloy, S-HT for smelted and heat-treated unrefined alloy, R2Mn for heat-treated and refined alloy with 2 wt% Mn, R9Ni for heat-treated and refined alloy with 9 wt% Ni, and R9Ni2Mn for heat-treated and refined alloy with 9 wt% Ni and 2 wt% Mn, respectively. The label "S/S-HT" is used to collectively refer to S and S-HT alloys when they exhibit similar behavior. The processing steps are summarized in **Figure 7**.

The equilibrium phase diagrams for the Fe–Cr–Ni–Co–Mn system as calculated with FactSage 8.3[43] are presented in **Figure 8**. All metallic phases from the Scientific Group Thermodata Europe (SGTE) intermetallic compound and alloy

© 2025 The Author(s). Steel Research International published by Wiley-VCH GmbH

1869344x, 0, Downloaded from https://onlinelibrary.wiley.com/doi/10.1002/srin.202500384 by Rwth Aachen University Zentraler Rechnungseingang, Wiley Online Library on [22/07/2025]. See the Terms and Conditions (https://onlinelibrary.wiley.com/terms-and-conditions) on Wiley Online Library for rules of use; OA articles are governed by the applicable Creative Commons License

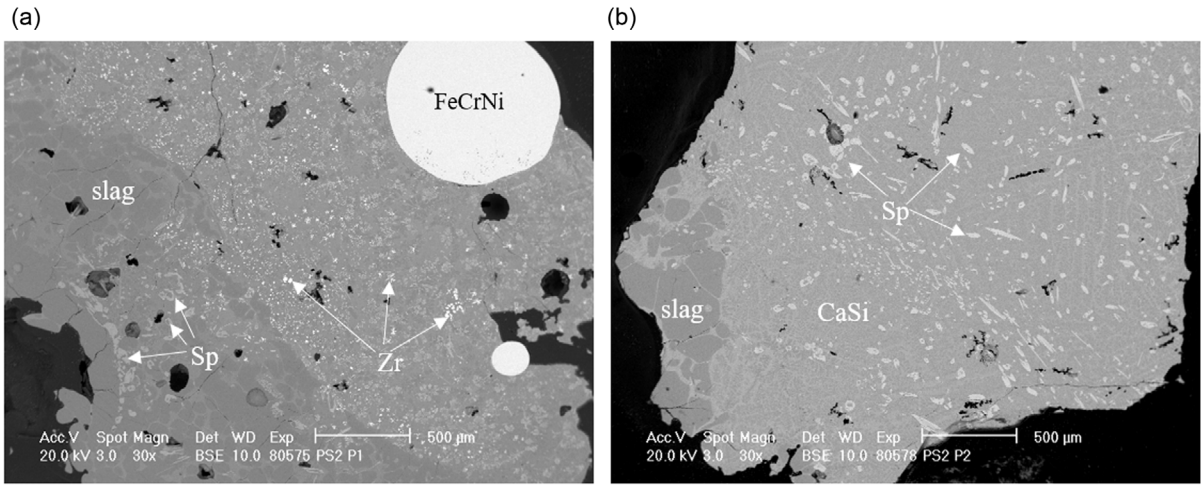

Figure 5. SEM-BSE images revealing the a) various phases in the slag microstructure, and highlighting, b) the intergrown spinel crystals within the slag matrix. The following naming scheme is used: Sp for spinels (mainly chromite), CaSi for Ca-rich silicates, Zr for zirconia, and FeCrNi for metallic inclusions with compositions close to either pure nickel or base alloy.

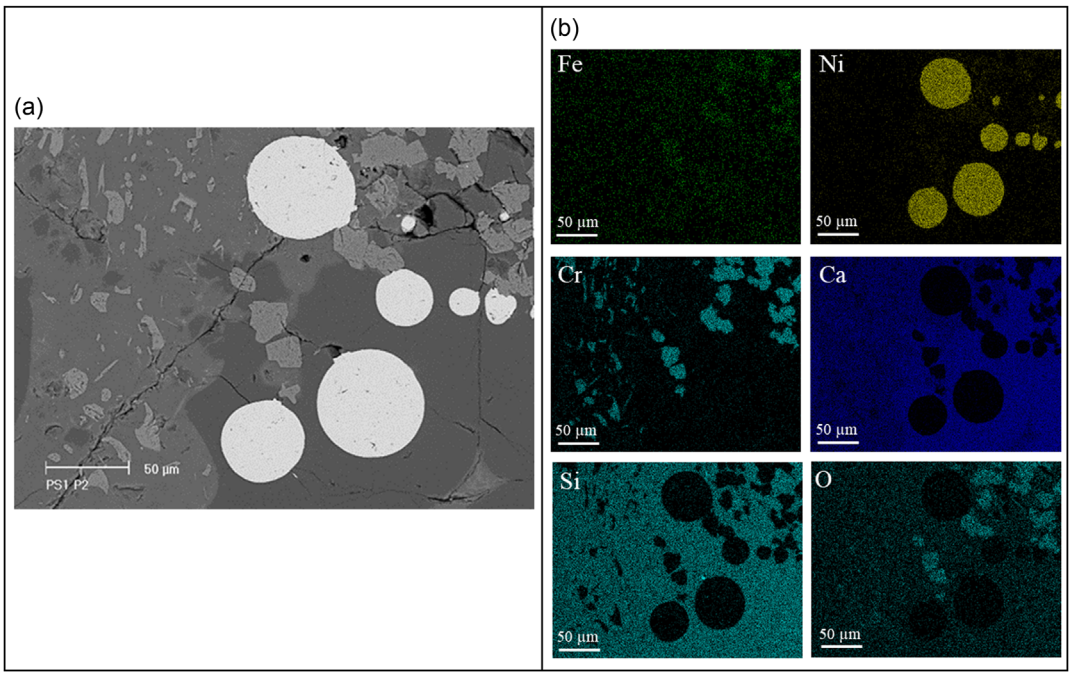

Figure 6. a) SEM-BSE image of a region of the slag and b) EDX elemental maps highlighting the presence of Ni droplets and Cr-rich spinels within the slag matrix.

solution databases[44] were incorporated in the calculation. The identified phases include austenite (γ), delta-ferrite (δ), alpha-ferrite (α), sigma (σ), chromium-rich alpha prime (α'), and nickel-rich gamma prime (γ'). Although such phases are predicted to be thermodynamically stable in the phase diagrams, they may not actually appear in the microstructure due to slow transformation kinetics or nonequilibrium conditions. For instance, the formation of α' and γ' phases has been reported to be only induced by neutron/ion irradiation[45,46] or prolonged aging treatments.[47]

The lower and upper temperature limits for single-phase austenite (γ), marked with pink stars in Figure 8, are as follows: S-HT: 785–1075, R2Mn: 755–1060, R9Ni: 750–1160, and R9Ni2Mn: 735–1180 °C. Notably, alloys with higher nickel content (R9Ni and R9Ni2Mn) have higher upper limits for the single-phase γ-austenite region, while increasing manganese alone, as in the case of R2Mn, does not produce a similar effect. In contrast, the lower stability limits remain consistent at around 750 °C, below which alpha-ferrite (α) starts to form.

© 2025 The Author(s). Steel Research International published by Wiley-VCH GmbH

1869344x, 0, Downloaded from https://onlinelibrary.wiley.com/doi/10.1002/srin.202500384 by Rwth Aachen University Zentraler Rechnungseingang, Wiley Online Library on [22/07/2025]. See the Terms and Conditions (https://onlinelibrary.wiley.com/terms-and-conditions) on Wiley Online Library for rules of use; OA articles are governed by the applicable Creative Commons License

Table 4. Elemental composition (in wt%) of studied alloys, and their corresponding Ni_{eq} and Cr_{eq} values. Commercial-grade AISI 304 steel is included as reference.

Alloy	Fe	Cr	Ni	Co	Mn	Si	Cu	C	S	Ni_{eq}	Cr_{eq}
S/S-HT	73.0	18.60	7.70	0.47	0.24	<0.003	<0.02	0.024	0.005	8.68	18.60
R2Mn	71.4	18.53	7.35	0.42	2.33	<0.003	<0.02	0.026	0.007	9.42	18.51
R9Ni	70.3	18.73	9.07	0.44	0.25	<0.003	<0.02	0.065	0.006	11.28	18.73
R9Ni2Mn	69.8	18.39	9.03	0.43	1.59	<0.003	<0.02	0.061	0.005	11.78	18.39
AISI 304[a)]	Bal.[b)]	17.0–19.0	8.0–10.5	–	≤2.00	≤1.00	–	≤0.07	≤0.015	8.0–14.0[c)]	17.0–20.5[c)]

[a)]Typical compositions from Euro Inox.[52] [b)]Difference from 100 wt%. [c)]Values calculated based on the typical AISI 304[41] compositions using Equations (1) and (2).

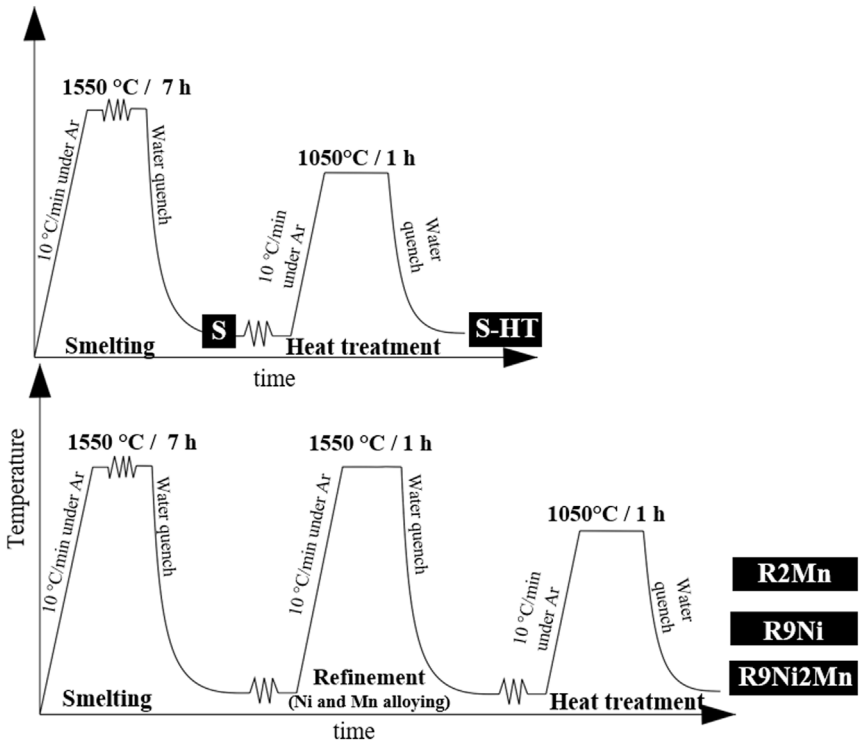

Figure 7. Processing paths for S, S-HT, R2Mn, R9Ni, and R9Ni2Mn alloys.

3.3. Microstructural Analysis of the Bulk Alloys

SEM-BSE images of polished cross sections of the alloys are shown in **Figure 9**, where austenite, ferrite, and martensite constituents can be qualitatively distinguished. The microstructure of the initial bulk alloy S (Figure 9a) revealed austenite and martensite phases within grains, with darker ferrite along the grain boundaries. The ferrite phases also exhibited skeletal features. After heat treatment, individual ferrite phases became more elongated (Figure 9b). They also appeared to have fragmented into smaller pieces, and the grain boundaries were less distinct. The addition of manganese did not visibly alter the microstructural characteristics within the grains, as observed in R2Mn (Figure 9c). The red inset in Figure 9c further highlights the lath-like morphologies inside the grains, which is a typical characteristic of martensite in low-carbon stainless steels.[48] In contrast, the microstructures of R9Ni and R9Ni2M showed an austenitic matrix, with ferrite as dispersed precipitates having spheroidal to vermicular morphologies (Figure 9d,e). Additionally, the ferrite fractions in the R9Ni and R9Ni2Mn were qualitatively less compared to the first two samples. Furthermore, a few $Cr_2(Mn,Fe)O_4$ particles (5–10 μm) were observed scattered across all the microstructures.

The microstructural characteristics can be partially explained by the differences in the solidification pathways of the alloys from the liquid phase to the solution annealing temperature (1050 °C), as illustrated by their corresponding phase diagrams in Figure 8. For the S-HT and R2Mn alloys, the sequence $L \rightarrow L + \delta \rightarrow \delta \rightarrow \delta + \gamma \rightarrow \gamma$ suggests first nucleation of δ-ferrite from the liquid phase and its complete solidification, followed by nucleation

© 2025 The Author(s). Steel Research International published by Wiley-VCH GmbH

1869344x, 0, Downloaded from https://onlinelibrary.wiley.com/doi/10.1002/srin.202500384 by Rwth Aachen University Zentraler Rechnungseingang, Wiley Online Library on [22/07/2025]. See the Terms and Conditions (https://onlinelibrary.wiley.com/terms-and-conditions) on Wiley Online Library for rules of use; OA articles are governed by the applicable Creative Commons License

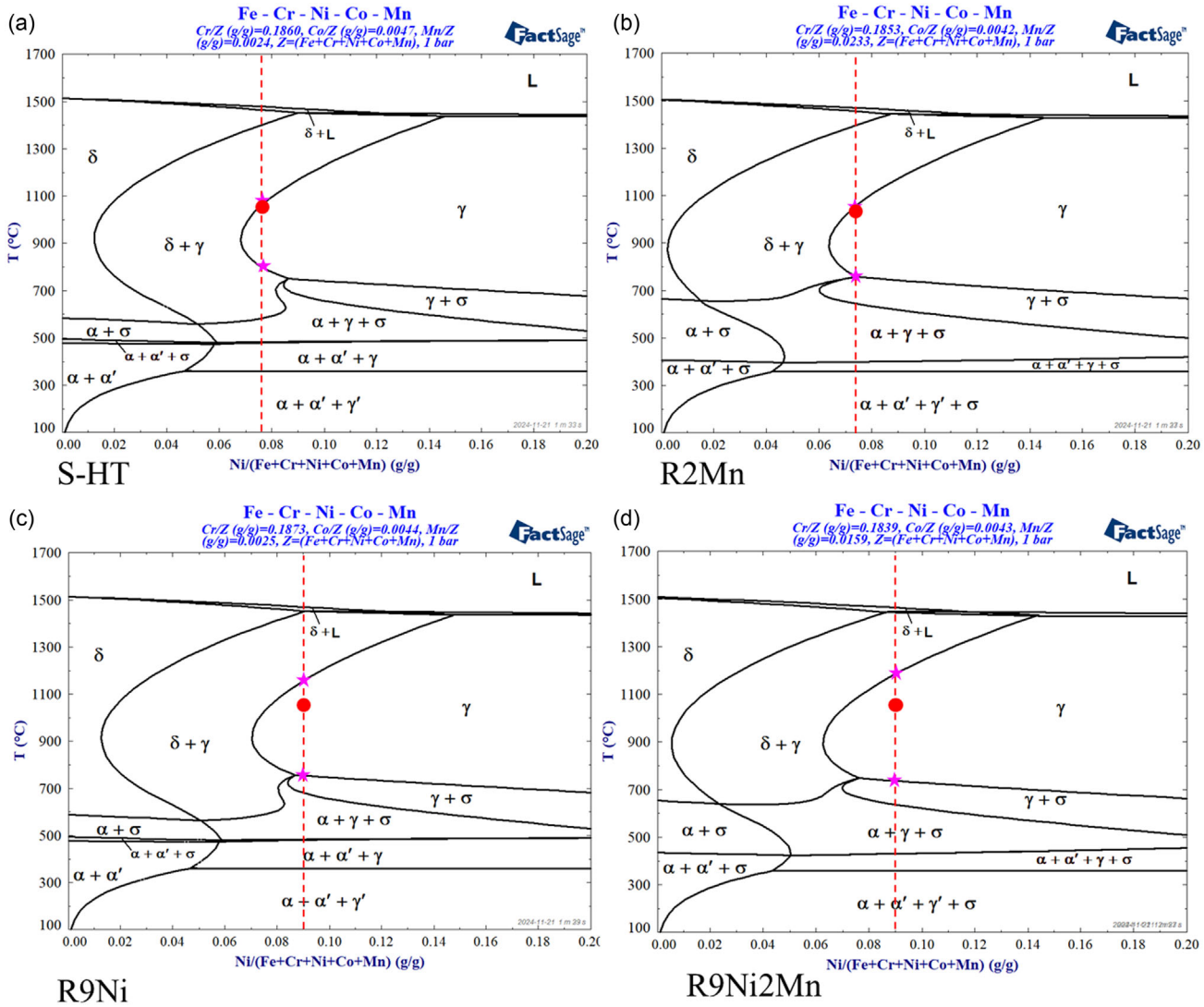

Figure 8. Calculated equilibrium phase diagrams from FactSage 8.3 using SGTE commercial database for a) S-HT, b) R2Mn, c) R9Ni, and d) R9Ni2Mn alloys. Phase designations are as follows: γ for austenite, δ for delta-ferrite, σ for sigma, α for alpha-ferrite, α' for Cr-rich alpha prime, and γ' for Ni-rich gamma prime. The red broken lines denote the position of the alloys, while the red-filled circles mark the point at the solution annealing temperature (1050 °C). The pink stars denote the upper and lower temperature limits for the single-phase γ-austenite stability region.

and growth of γ-austenite from the δ-ferrite grains. This would have resulted in a microstructure of austenite grains embedded within a skeletal ferrite matrix. On the other hand, the R9Ni and RNi2Mn alloys follow the pathway $L \rightarrow \delta + \gamma \rightarrow \gamma$, which suggests simultaneous nucleation and growth of δ-ferrite and γ-austenite directly from the liquid phase. The solid-state transformation ($\delta \rightarrow \gamma$) leads to chromium enrichment and nickel depletion in the remaining δ-ferrite grains as they decrease in size while γ-austenite grains are growing. Since R9Ni and R9Ni2Mn have compositions located deeper within the single-phase γ-austenite region compared to the S-HT and R2Mn alloys (Figure 8), their microstructures are expected to contain a higher fraction of austenite. Although the phase diagrams predict single-phase γ-austenite at 1050 °C, small amounts of δ-ferrite phases may remain undissolved due to nonequilibrium cooling.

The elemental compositions of the phases were determined based on the average of 3–5 EDX measurements, with the results listed in **Table 5**. Since martensite was expected to have identical compositions with its parent phase austenite, they were not distinguished in the analysis. The austenite/martensite phases had consistently higher content of nickel (by ≈5 wt%) and iron (by ≈2–3 wt%), but lower amounts of chromium (by ≈7–9 wt%) compared to the ferrite phase. Additionally, the cobalt content was slightly higher in the austenite/martensite phase. Manganese concentration was also slightly higher in these phases, but only particularly evident in alloys with elevated manganese levels (R2Mn and R9Ni2Mn).

The phase area fractions were determined by overlaying the EBSD phase maps with the EDX elemental maps. This approach is demonstrated for the sample "S" in **Figure 10**. The EBSD

© 2025 The Author(s). Steel Research International published by Wiley-VCH GmbH

1869344x, 0, Downloaded from https://onlinelibrary.wiley.com/doi/10.1002/srin.202500384 by Rwth Aachen University Zentraler Rechnungseingang, Wiley Online Library on [22/07/2025]. See the Terms and Conditions (https://onlinelibrary.wiley.com/terms-and-conditions) on Wiley Online Library for rules of use; OA articles are governed by the applicable Creative Commons License

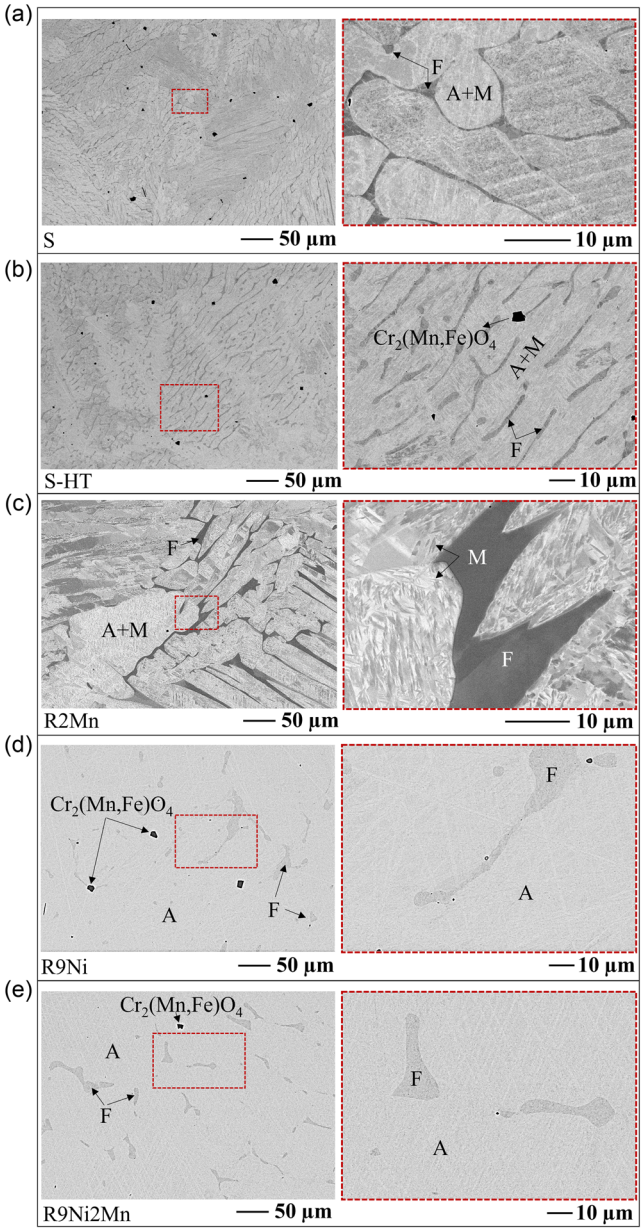

Figure 9. Microstructural SEM-BSE images of polished specimens from a) S, b) S-HT, c) R2Mn, d) R9Ni, and e) R9Ni2Mn alloys, highlighting the morphologies and qualitative area fractions of austenite (A), ferrite (F), and martensite (M) phase constituents. $Cr_2(Mn,Fe)O_4$ oxide inclusions are also visible within the microstructures.

phase map can distinguish between phases with FCC and BCC structures (Figure 10b). Consequently, γ-austenite can be straightforwardly quantified based on the FCC area fraction. The remaining phases were indexed as BCC-Fe and are attributed to ferrite and martensite phases. Although martensite has a body-centered tetragonal (BCT) structure, its low tetragonality (see also Section 3.5) makes it difficult to distinguish from ferrite by EBSD. The δ-ferrite phase can be distinguished from α-ferrite or martensite by EDX mapping due to its higher Cr concentration and lower Ni and Fe concentrations (Figure 10c). By combining the EBSD phase map with EDX data, such as with a Cr elemental map, the three phases can now be effectively distinguished and quantified in terms of their area fractions (Figure 10d).

The kernel averaged misorientation (KAM) map (Figure 10e) additionally revealed significantly higher KAM values for the martensite phase, attributed to its strained nature. On the other hand, ferrite exhibited low local misorientation (<0.4°), indicative of a phase that is formed and stabilized at elevated temperatures. This finding supports the assumption that δ-ferrite, rather than α-ferrite, was present within the microstructure of the investigated alloys.

The EDX elemental maps of Cr and Ni, EBSD phase maps, and combined EDX-EBSD maps of the investigated alloys are shown in **Figure 11**, and the corresponding phase area fractions are summarized in **Figure 12**. The findings indicate that austenite fractions increased from S to S-HT alloy, while ferrite fractions remained the same. Furthermore, a slight increase in austenite content was observed with manganese addition in the case of R2Mn. However, the R2Mn alloy had higher ferrite content compared to S/S-HT alloys. One possible explanation for this is the behavior of manganese in chromium–nickel containing steels. Although Mn is a good austenite stabilizer against martensite formation, it is reported to be less effective in preventing the formation of ferrite phases compared to Ni.[33] On the other hand, R9Ni and R9Ni2Mn exhibited a predominant austenitic microstructure. Notably, ferrite phases were still present in these alloys, constituting 2.6% and 3.9% of the total area.

Table 5. Chemical compositions of the phases within the bulk alloys (a: austenite, M: martensite, and F: ferrite), based on the average of 3–5 EDX point measurements per phase.

Alloy	Phase	Composition [wt%]				
		Fe	Cr	Ni	Co	Mn
S	A/M	71.7 ± 0.5	18.8 ± 0.1	8.2 ± 0.3	0.97 ± 0.06	0.30 ± 0.10
	F	69.3 ± 0.1	25.9 ± 0.1	3.6 ± 0.2	0.83 ± 0.15	0.30 ± 0.00
S-HT	A/M	71.3 ± 0.3	19.2 ± 0.2	8.3 ± 0.4	0.87 ± 0.06	0.23 ± 0.06
	F	67.7 ± 0.4	28.1 ± 0.4	3.4 ± 0.1	0.60 ± 0.00	0.25 ± 0.07
R2Mn	A/M	70.4 ± 0.2	18.6 ± 0.1	8.3 ± 0.3	0.97 ± 0.06	1.80 ± 0.00
	F	67.9 ± 0.3	25.6 ± 0.1	4.2 ± 0.1	0.83 ± 0.06	1.53 ± 0.06
R9Ni	A/M	70.9 ± 0.4	18.9 ± 0.1	9.1 ± 0.4	0.77 ± 0.12	0.37 ± 0.06
	F	68.7 ± 0.1	26.1 ± 0.2	4.4 ± 0.1	0.67 ± 0.06	0.23 ± 0.06
R9Ni2Mn	A/M	69.6 ± 0.3	18.2 ± 0.3	9.6 ± 0.4	0.80 ± 0.10	1.83 ± 0.06
	F	67.3 ± 0.2	26.1 ± 0.2	4.3 ± 0.1	0.73 ± 0.06	1.53 ± 0.06

3.4. Microindentation Results

One limitation of the combined EDX-EBSD phase quantification approach is that the selected region may not be representative of the overall microstructure. In order to check the validity of the obtained phase area fractions, HV values were taken at randomly chosen areas across larger regions (≈1 cm^2) of the samples. **Figure 13**a shows the HV values of the alloys plotted against load. Accordingly, HV values exhibited an asymptotic decrease with

© 2025 The Author(s). Steel Research International published by Wiley-VCH GmbH

1869344x, 0, Downloaded from https://onlinelibrary.wiley.com/doi/10.1002/srin.202500384 by Rwth Aachen University Zentraler Rechnungseingang, Wiley Online Library on [22/07/2025]. See the Terms and Conditions (https://onlinelibrary.wiley.com/terms-and-conditions) on Wiley Online Library for rules of use; OA articles are governed by the applicable Creative Commons License

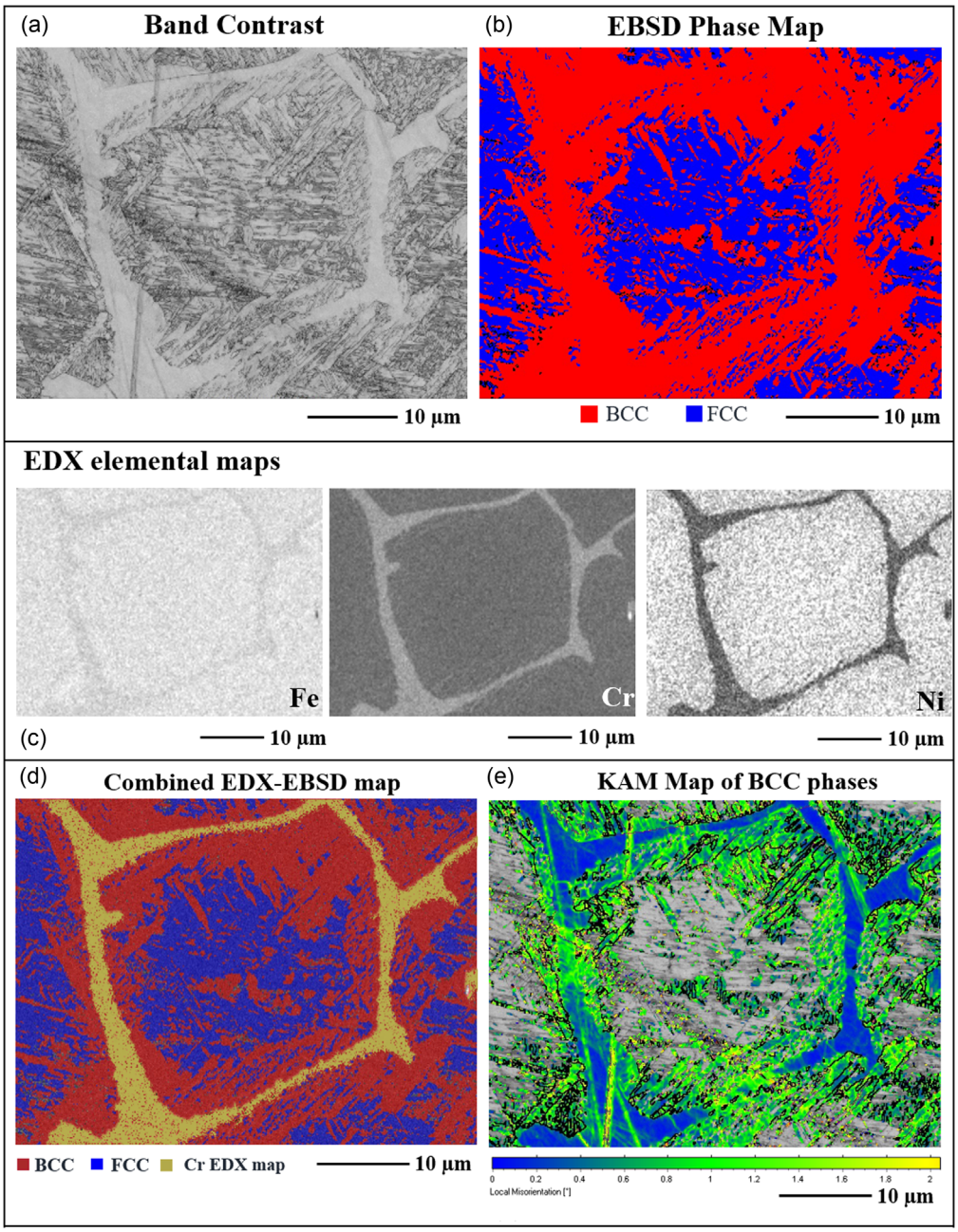

Figure 10. a) Band contrast image, b) EBSD phase map, and c) EDX elemental maps from a region in the sample S. The area fractions of ferrite, austenite, and martensite phases were quantified from the d) combined EDX-EBSD maps; and e) KAM map of the BCC phases, showing the presence of highly misoriented martensitic phase and low-misoriented ferrite phases.

increasing load until a plateau beyond 700 mN was reached. This behavior was consistent with the literature findings, wherein the influence of individual phases, defects, and surface roughness diminishes as indentation size increases.[49] Expectedly, nearly constant "bulk" HV values with decreased deviation were attained at greater penetration depths. Figure 13b illustrates a decrease in bulk HV values with increasing austenite fractions, with R9Ni2Mn exhibiting the lowest mean value at 162. This observation is aligned with the common view that coexisting austenite is softer than martensite.[50,51] Although R9Ni was predominantly austenitic like R9Ni2Mn, it demonstrated the highest HV standard deviation. While this phenomenon cannot be completely explained in this study, it may be attributed to a high phase inhomogeneity across a region larger than that covered by combined EDX-EBSD maps and/or to a dynamic transformation of austenite to martensite during testing (**Figure 14**). Notably, the HV values of R9Ni2Mn fell within the typical ranges for solution-annealed AISI 304 steels (140–200),[52] indicating high austenitic phase homogeneity and stability, and comparable hardness with the target steel.

© 2025 The Author(s). Steel Research International published by Wiley-VCH GmbH

1869344x, 0, Downloaded from https://onlinelibrary.wiley.com/doi/10.1002/srin.202500384 by Rwth Aachen University Zentraler Rechnungseingang, Wiley Online Library on [22/07/2025]. See the Terms and Conditions (https://onlinelibrary.wiley.com/terms-and-conditions) on Wiley Online Library for rules of use; OA articles are governed by the applicable Creative Commons License

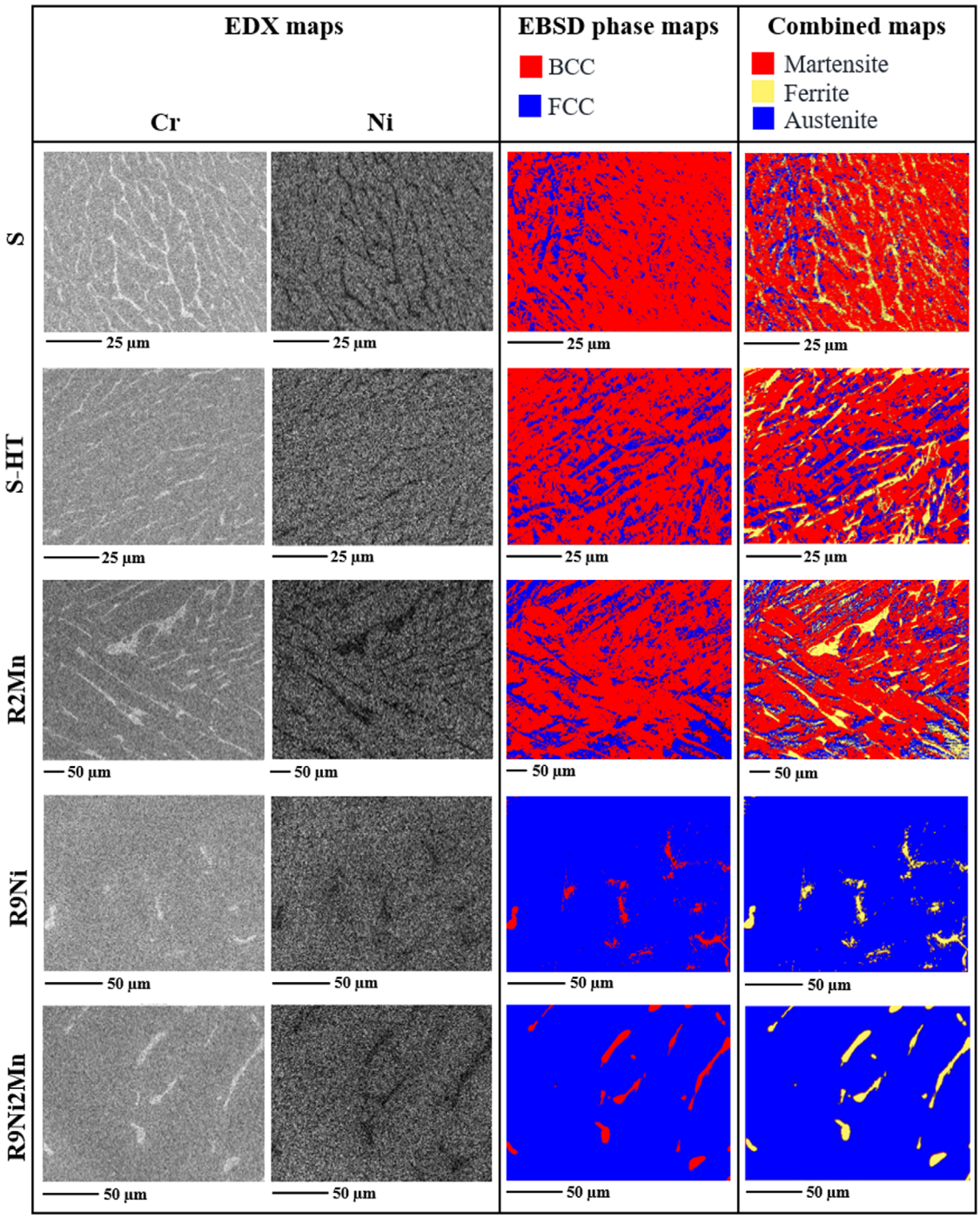

Figure 11. EDX elemental maps, EBSD phase maps, and combined EDX-EBSD maps of the S, S-HT, R2Mn, R9Ni, and R9Ni2Mn alloys.

3.5. Martensitic Phase Evolution

Martensitic transformations were investigated by identifying the temperatures at which the BCC (110) peak surpasses the background noise in the HT-XRD patterns during controlled slow cooling. However, this method is limited as it cannot reliably distinguish between martensite and ferrite phases due to the low tetragonal characteristic of the martensite phase formation in combination with peak broadening due to microstrain. Peak splitting of cubic ferrite Bragg reflections into tetragonal martensite Bragg reflections (e.g., 200_{BCC} into 200_{BCT} and 002 $_{BCT}$) cannot be observed. This was evident in sample "S", where the calculated c/a ratio derived from the d-spacings (d_{002}/d_{200}) was less than 1.005 (see Figure S2,

© 2025 The Author(s). Steel Research International published by Wiley-VCH GmbH

1869344x, 0, Downloaded from https://onlinelibrary.wiley.com/doi/10.1002/srin.202500384 by Rwth Aachen University Zentraler Rechnungseingang, Wiley Online Library on [22/07/2025]. See the Terms and Conditions (https://onlinelibrary.wiley.com/terms-and-conditions) on Wiley Online Library for rules of use; OA articles are governed by the applicable Creative Commons License

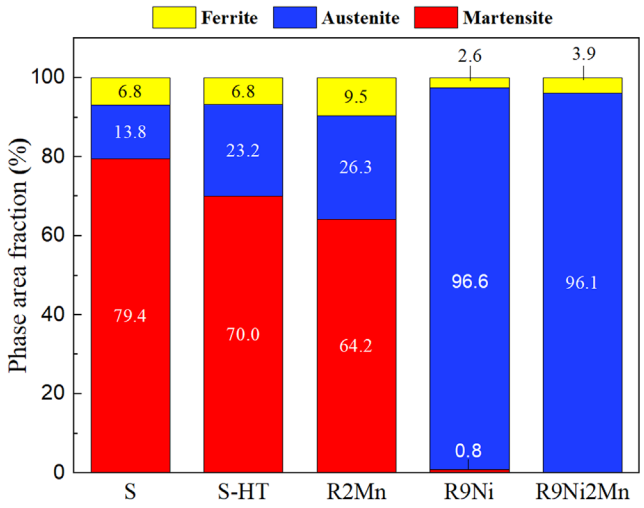

Figure 12. Phase area fractions (%) based on the combined EDX-EBSD phase quantification method.

Supporting Information). This characteristic aligned with expectations, as higher carbon contents (>0.18 wt% C in plain steels) are required to stabilize[51] BCT-martensite, which was not met in the investigated alloys. As ferrite phases were presumed to be minor compared to martensite based on the results in Figure 12, the BCC peak in HT-XRD patterns was attributed to martensite and used to estimate martensite evolution temperatures.

The martensite start temperature (M_s) in austenitic steels is associated with the diffusionless and athermal transformation of austenite into martensite.[38] It is influenced by several factors, including chemical compositions,[53,54] prior austenite grain sizes,[55] morphology of martensitic phases,[56] as well as the austenitizing temperatures and cooling rates.[57] Numerous empirical equations have been developed to estimate M_s, such as Dai et al.[54] which developed the following equation on the basis of chemical compositions in wt%.

$$M_s(°C) = 501 - 199.8(C + 1.4N) - 17.9Ni - 21.7Mn - 6.8Cr - 45Si - 55.9Mo - 1.9C(Mo + Cr + Mn) - 14.4[(Ni + Mn)(Cr + Mo + Al + S9)]^{1/2} \quad (4)$$

In the case of austenitic stainless steels, M_s is generally near or below 0 °C; hence, austenite remains stable at room temperature.[37] **Table 6** shows a summary of the calculated M_s for the investigated alloys based on equation (4). For AISI 304, the composition that was used for calculation corresponds to its maximum tolerance limits in Table 4. Notably, only the S/S-HT alloy exhibits a calculated M_s above 0 °C, while the other alloys have M_s that are near or below 0 °C.

For an accurate M_s determination, extensive experimental work is required, such as combined dilatometry experiments and hardness tests at varying cooling rates,[58] as well as verification of phase fractions with various methods like XRD, EBSD, magnetic methods, and metallographic analyses.[37,59,60] Consequently, HT-XRD analysis alone can only provide the observable and relative martensitic transformation temperatures, which may not directly correspond to the exact M_s.

The HT-XRD contour plot, shown in **Figure 15**, reveals the temperature ranges where BCC phases begin to form. The shifting of reflections was due to thermal contractions with cooling. The analysis was focused on the FCC (111) and BCC (110) reflections within the narrow range of 42.5°–45° 2θ Cu Kα, as they represent the main FCC and BCC peaks in steels.[40] Concentration on this range was needed to significantly reduce the scanning time required for continuous cooling, while ensuring that the important phase transformation data is captured. **Table 7** summarizes the estimated onset of BCC formation across the investigated alloys. Accordingly, BCC formation occurred at the highest temperature in alloy R2Mn, followed by S/S-HT, R9Ni, and R9Ni2Mn. Nevertheless, the martensitic evolution ranges were deemed relatively close across the investigated alloys. On the other hand, the intensity of the BCC peak, correlated to the fraction of martensite phase forming as a function of temperature, varied significantly in the following

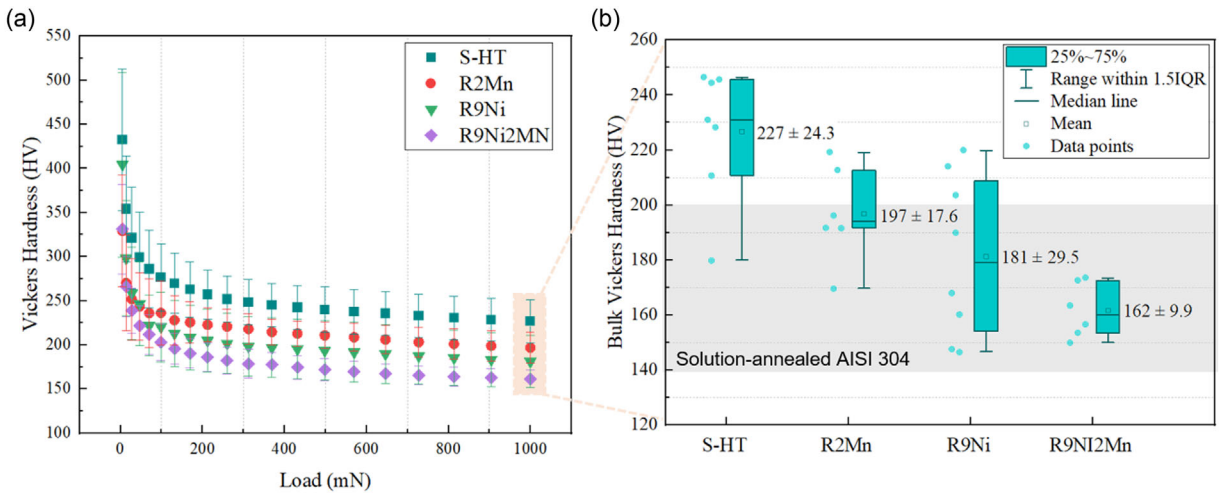

Figure 13. a) HV values of the studied alloys plotted against load; b) box plot of the "bulk" HV values obtained at 1000 mN, with mean values and standard deviations as labeled. Typical range for solution-annealed AISI 304 steels is included as ref.[52].

© 2025 The Author(s). Steel Research International published by Wiley-VCH GmbH

1869344x, 0, Downloaded from https://onlinelibrary.wiley.com/doi/10.1002/srin.202500384 by Rwth Aachen University Zentraler Rechnungseingang, Wiley Online Library on [22/07/2025]. See the Terms and Conditions (https://onlinelibrary.wiley.com/terms-and-conditions) on Wiley Online Library for rules of use; OA articles are governed by the applicable Creative Commons License

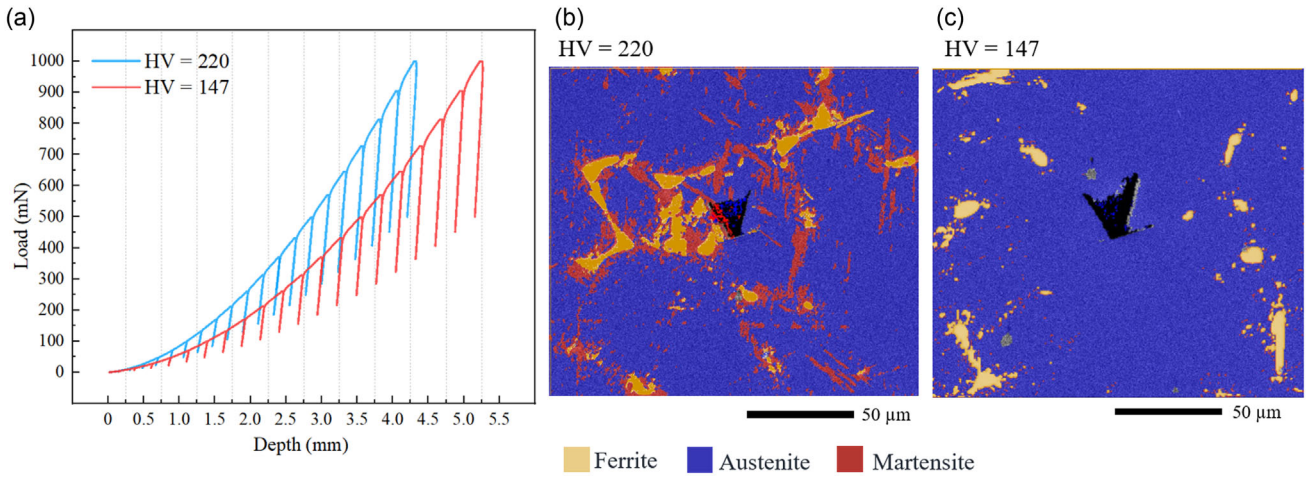

Figure 14. a) Plot of load against depth showing two indentation curves yielding different hardness values (HV = 220 and HV = 147); phase map of the region with the b) higher and c) lower HV values.

Table 6. Calculated M_s temperatures and final FCC-BCC phase fractions.

Alloy	M_s [°C]
S/S-HT	50.7
R2Mn	−6.7
R9Ni	0.1
R9Ni2Mn	−36.1
AISI304*	−102.6

decreasing order: S/S-HT, R2Mn, R9Ni, and finally R9Ni2Mn. Martensite appeared to form at temperatures higher than ambient for all studied alloys. However, the martensitic evolution was delayed in alloys R9Ni and R9Ni2Mn, resulting in austenite retention at room temperature.

The XRD patterns of the alloys in their final state (**Figure 16**) indicate the presence of FCC reflections corresponding to austenite and BCC reflections related to martensite in the studied alloys. Qualitative estimation of the intensities suggests the presence of retained austenite in the following decreasing order: R9Ni2Mn, R9Ni, R2Mn, and S/S-HT. Small amounts of Cr_2O_3 and Fe_3O_4 oxides were consistently detected, likely due to minor oxidation of the alloys even under high vacuum conditions.

4. Discussion

4.1. Properties of Recycled Steels

Based on the present findings, smelting an end-of-life Jülich F10 stack interconnect assembly produced a steel that was within the typical compositional range of AISI 304, except for a slightly lower Ni content. The as-cast steel exhibited a predominantly martensitic microstructure. To achieve the desired microstructure, the steel was alloyed with austenite-stabilizing elements. Increasing the nickel and manganese contents to reach 9 wt% Ni and 2 wt% Mn resulted in a microstructure consisting of 96% austenite with 4% δ-ferrite. Based on the calculated phase diagram and microstructural observations, the residual δ-ferrite likely resulted from the incomplete solid-state transformation of ferrite to austenite during nonequilibrium cooling, combined with insufficient heat treatment. This duplex-like microstructure is not unexpected in cast and welded austenitic stainless steels.[61,62] In commercial practice, the residual δ-ferrite can be further minimized with adequate thermal processing techniques, like in slab casting.[61] It is important to note that the presence of minor δ-ferrite could be beneficial, as austenitic stainless steels can contain up to 10% δ-ferrite for improved yield and tensile strengths.[34]

Microindentation tests showed that the 9 wt% Ni–2 wt% Mn steel had precise HV values falling within the typical range for AISI 304. High-temperature XRD confirmed that its M_s range was slightly above room temperature, indicating the presence of metastable austenite. This behavior is consistent with that of cast AISI 304, where metastable austenite can transform to martensite through mechanisms such as the TRIP effect.[34,37]

Thus, the 9 wt% Ni–2 wt% Mn recycled steel closely matched the compositional, microstructural, mechanical (hardness), and thermophysical (M_s) properties of AISI 304. Further mechanical tests (e.g., for determining elastic modulus, yield, and tensile strength) are, however, recommended to confirm its suitability for AISI 304 applications. Additionally, since AISI 304 is also applied in mildly corrosive environments, the corrosion resistance of the recycled steel should be tested using standard methods such as salt spray testing and electrochemical polarization.[63,64]

The presence of δ-ferrite in the recycled steel, however minor, may render it unsuitable in applications requiring strict nonmagnetic behavior. That said, magnetic tests such as ferritescope[37] are recommended to quantify its ferromagnetic property, from which it may have to be classified as a variant of the standard nonmagnetic grade.

4.2. Cobalt Contamination

The recycled steels were found to contain ≈0.40 wt% cobalt. Cobalt has been traditionally regarded as an unavoidable residual

© 2025 The Author(s). Steel Research International published by Wiley-VCH GmbH

1869344x, 0, Downloaded from https://onlinelibrary.wiley.com/doi/10.1002/srin.202500384 by Rwth Aachen University Zentraler Rechnungseingang, Wiley Online Library on [22/07/2025]. See the Terms and Conditions (https://onlinelibrary.wiley.com/terms-and-conditions) on Wiley Online Library for rules of use; OA articles are governed by the applicable Creative Commons License

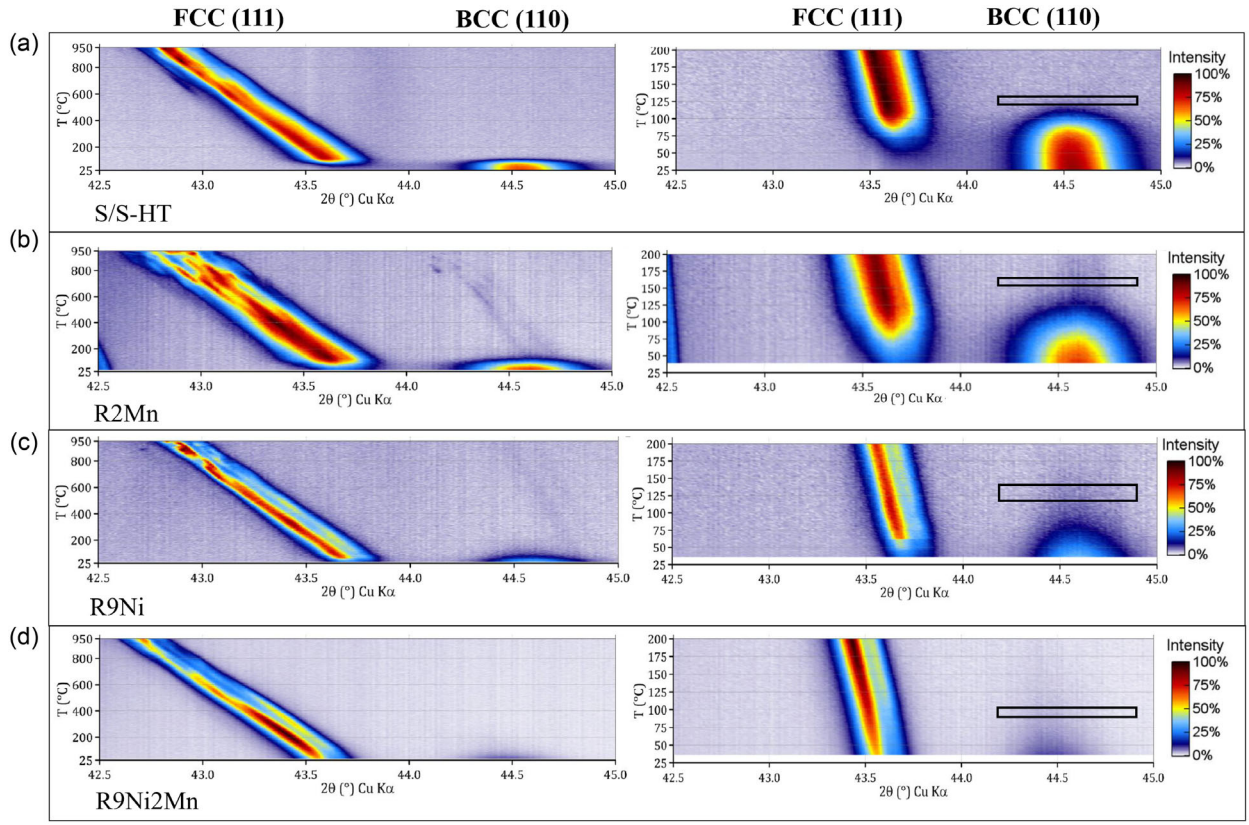

Figure 15. HT-XRD contour plots (left) and corresponding zoomed-in views (right) showing the intensity evolution of FCC (111) and BCC (110) reflections upon cooling from 950 °C to room temperature at 2 °C min^{-1} for: a) S/S-HT, b) R2Mn, c) R9Ni, and d) R9Ni2Mn alloys. The estimated onset temperatures for BCC (110) phase formation are indicated by black boxes in the zoomed-in plots.

Table 7. Temperature ranges corresponding to onset of BCC (110) formation from Figure 15.

Alloy	Onset of BCC (110) formation [°C]
S/S-HT	125–130
R2Mn	150–160
R9Ni	120–140
R9Ni2Mn	80–100

element in austenitic stainless steels, typically present at levels below 0.3 wt% and commonly not listed in standard chemical composition datasheets.[65] However, with cobalt's recent classification as a category 1B carcinogen, steels containing more than 0.1 wt% Co are now required to carry appropriate warning labels for certain applications, such as medical devices, as mandated by the EU Medical Device Regulation (MDR).[65,66] This, in turn, creates a strong incentive to minimize cobalt traces in steels. However, cobalt removal poses difficulty due to its preferential partitioning into the melt over the slag under conventional steelmaking conditions.[30] While alloy dilution could further reduce the cobalt content to acceptable levels, e.g., via the addition of primary iron, ferronickel, or ferrochromium, it is not a favorable solution from a circular economy perspective. Cobalt is classified as a critical raw material in the EU due to its important role in applications such as EV battery production.[67,68] Thus, prioritizing its recovery from end-of-life streams is crucial. Since cobalt is a component of the interconnect coating material, developing efficient decoating methods must be explored. This could be done chemically, such as through acid pickling, or mechanically via abrasive blasting and mechanical grinding.[28]

4.3. Industrial Integration of SOC Interconnect Recycling

Linear projection of the stack weights from Harboe et al.[14] suggests that the manufacturing of 1-GW capacity of Jülich F20 stacks would result in roughly 32 000 metric tonnes of scrap ferritic steels and nickel meshes. With expected SOC stack installed capacities of 1,000 GW by 2045,[69] this scrap volume will substantially increase. However, similar to other secondary steel sources,[27] it will take time before sufficient quantities accumulate to support a self-sustaining recycling route. Consequently, blending SOC stack scraps with other end-of-life steels will be necessary. In this process, scrap quality control is essential as it can impact the microstructural and mechanical properties of product steels, and therefore, determines the possible steel grades.[70] The chemical composition of the recycled steels (see Table 4) classifies them as "clean" secondary sources due to their low concentrations of elements typically considered detrimental to austenitic steels, such as carbon,[71] sulfur,[35,72]

© 2025 The Author(s). Steel Research International published by Wiley-VCH GmbH

1869344x, 0, Downloaded from https://onlinelibrary.wiley.com/doi/10.1002/srin.202500384 by Rwth Aachen University Zentraler Rechnungseingang, Wiley Online Library on [22/07/2025]. See the Terms and Conditions (https://onlinelibrary.wiley.com/terms-and-conditions) on Wiley Online Library for rules of use; OA articles are governed by the applicable Creative Commons License

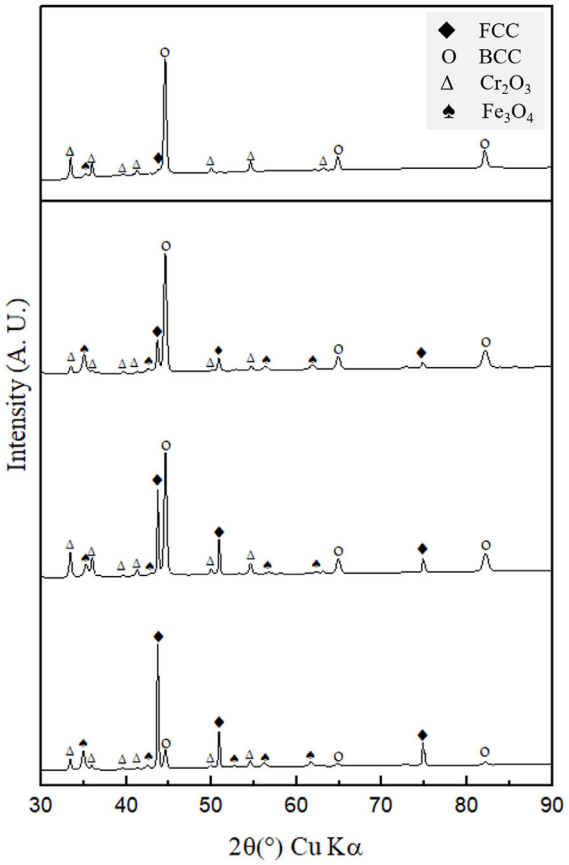

Figure 16. XRD patterns of the alloys in their final state. Reflections corresponding to the FCC phases are indicated by filled diamond, the BCC phases by open circles, the Cr_2O_3 phase by open triangles, and the Fe_3O_4 by filled spades.

silicon,[35] and copper.[73,74] This allows these materials to tolerate mixing with dirtier scraps for stainless steel production.

With minor alloying element additions, AISI 304 steels could be produced from interconnect assemblies without the need for primary iron addition, thereby enabling steel circularity. This approach is particularly attractive in a carbon-neutral scenario.

The overview of the proposed recycling pathway of Jülich F10 stack interconnect assemblies based on the current findings is presented in **Figure 17**. Since the current standard interconnect materials are ferritic steel-based,[21] the proposed recycling approach could be broadly applied to other SOC stack manufacturers as well. However, variations in the interconnect composition with stack design, choice of steel, and coating materials, nickel mesh content, as well as the presence of end-of-life contaminants must be considered. For such reasons, further research is needed to assess the recyclability of other SOC stack types.

4.4. Slag Management

Scaling up the proposed recycling approach requires careful management of slag, a byproduct typically generated at ≈60 to 270 kg per metric tonne of EAF steel produced.[75] Furthermore, effective slag management should focus on potential chromium recovery pathways. Chromium, a key element in the slag, has a high affinity for oxygen, leading to its incorporation into stable oxide phases such as Cr-bearing spinel. There is the potential to recover these spinels mechanically from the slag system, especially when the crystal size has been tailored similarly with engineered artificial minerals for Li-Aluminate.[76,77] Thus, to maximize chromium recovery and minimize losses to nonrecoverable phases, the slag basicity, heating, and cooling conditions must be carefully

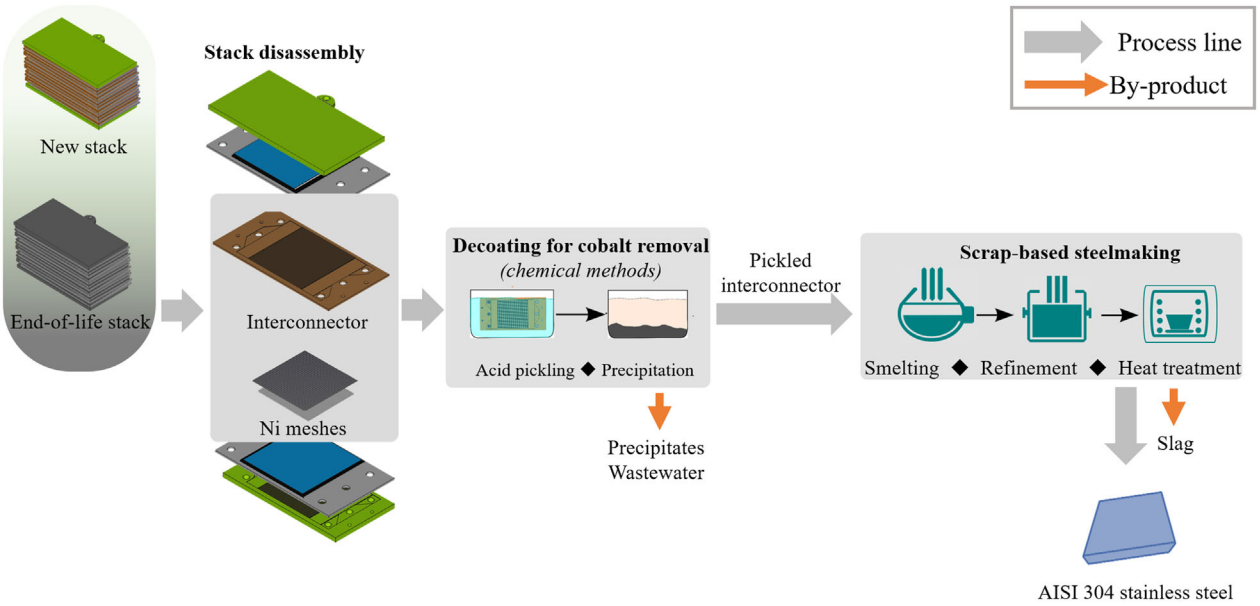

Figure 17. Schematic diagram of the proposed recycling pathway for Jülich SOC F10 stack interconnect assemblies.

© 2025 The Author(s). Steel Research International published by Wiley-VCH GmbH

1869344x, 0, Downloaded from https://onlinelibrary.wiley.com/doi/10.1002/srin.202500384 by Rwth Aachen University Zentraler Rechnungseingang, Wiley Online Library on [22/07/2025]. See the Terms and Conditions (https://onlinelibrary.wiley.com/terms-and-conditions) on Wiley Online Library for rules of use; OA articles are governed by the applicable Creative Commons License

controlled. Higher basicity promotes the chromium stabilization in spinel phases. Controlled slow cooling is another critical factor, as it promotes the growth of larger spinel-phase grains, simplifying mechanical separation methods for these phases. Additionally, total inclusions, which are about 2 vol% at laboratory-scale conditions, are expected to decrease with upscaling, resulting in fewer metallic inclusions and less contamination from refractory materials.

4.5. Material Downcycling

Although the proposed recycling approach yields high-demand AISI 304 steels, these may be considered as a functional downgrade from Crofer 22 APU, which is specially designed for high-temperature SOC applications.[21] Consequently, this approach may result in a reduction of material value in the context of SOC stack recycling.

To retain the functional value of Crofer, future studies should focus on the selective recovery of Crofer for reuse in the production of new SOC stacks. Scrap Crofer could be remelted into new sheets, while the detached meshes could be used as an alloying element in nickel-containing alloys. However, effective mechanical separation of the Crofer and meshes poses a challenge, as they are often heavily soldered and/or sintered together, making clean detachment difficult.[21,76] Additionally, since the standard Crofer contains negligible nickel,[78] the impact of nickel contamination on the performance of recovered Crofer remains unclear.

5. Conclusion

The feasibility of AISI 304 steel production through scrap-based steelmaking of end-of-life Jülich SOC F10 stack interconnect assemblies was demonstrated in the present study. The following conclusions were drawn based on the findings. 1) A base alloy with high metal yield and compositional homogeneity was achieved after smelting that utilized a basic oxide flux. Slag composition showed a significant presence of Cr (5.28 wt% Cr_2O_3), while a minor presence of Fe (1.46 wt% Fe_2O_3) and Mn (1.16 wt% MnO). Slag characterization revealed the presence of chromite spinels, which play a crucial role in chromium deportation, aligning with findings from the previous study.[19] 2) The base alloy as well as the refined alloy with higher manganese content (2 wt% Mn) showed microstructures with distinct grains constituted of martensite and austenite, and ferrite phases along the grain boundaries. On the other hand, refined alloys with higher nickel (9 wt% Ni) and both higher nickel and manganese concentrations (9 wt% Ni–2 wt% Mn) exhibited austenitic microstructures with dispersed spheroidal to vermicular ferrite phases. These microstructural characteristics can be explained by the solidification pathways from their calculated equilibrium phase diagrams. 3) The combined EDX-EBSD phase quantification method was used to determine the phase area fractions of the studied alloys. Based on this approach, an austenitic microstructure with less than 4% δ-ferrite was achieved in refined alloy with higher nickel (9 wt% Ni), as well as with higher nickel and manganese (9 wt% Ni–2 wt% Mn). 4) Bulk HV values decreased with increasing nickel and manganese additions, attributed to the increasing fraction and homogeneity of the austenite phase. Furthermore, refined alloy (9 wt% Ni–2 wt% Mn) possessed bulk HV values within the typical range for AISI 304 steels. 5) The relative M_s values were slightly higher than room temperature in all studied alloys. Nevertheless, the austenite phases of refined alloys (9 wt% Ni) and (9 wt% Ni–2 wt% Mn) were retained at room temperature, attributed to relatively slow martensitic evolution as a function of temperature.

Supporting Information

Supporting Information is available from the Wiley Online Library or from the author.

Acknowledgements

The authors gratefully acknowledge the contributions of the following colleagues from Forschungszentrum Jülich and Technische Universität Bergakademie Freiberg: F. Schulze-Küppers for the provision of SOC stacks, V. Gutzeit and J. Bartsch for their assistance with the metallographic sample preparation, E. Yazhenskikh for the guidance with thermodynamic equilibrium calculations, E. Wessel and G. Schmidt for the microstructural analyses, M. Ziegner for the high-temperature X-ray diffraction experiments and analyses, R. Möckel and D. Ebert for X-ray fluorescence analyses, and N. Menzler, S. Sarner, and R. Jacob for their valuable insights and discussions. The authors also acknowledge the funding received from the German Federal Ministry of Education and Research (BMBF) under the ReNaRe project with grant no. FKZ 03HY111J.

Open Access funding enabled and organized by Projekt DEAL.

Conflict of Interest

The authors declare no conflict of interest.

Data Availability Statement

The data that support the findings of this study are available in the supplementary material of this article.

Keywords

AISI 304, austenitic stainless steels, interconnects, recycling, scrap-based steelmaking, solid oxide cell stacks

Received: April 23, 2025
Revised: June 15, 2025
Published online:

[1] IEA, Net Zero Roadmap A Global Pathway to Keep the 1.5 °C Goal in Reach, https://www.iea.org/reports/net-zero-roadmap-a-global-pathway-to-keep-the-15-0c-goal-in-reach (accessed: February 2024).
[2] IRENA, Global hydrogen trade to meet the 1.5°C climate goal: Part I, https://www.irena.org/publications/2022/Jul/Global-Hydrogen-Trade-Outlook (accessed: April 2023).
[3] Dechema, acatech, Länderanalyse: Internationale Wasserstoff-Strategien im Vergleich, https://www.wasserstoff-kompass.de/news-media/dokumente/wasserstoff-strategien-laender-vergleich (accessed: April 2024).

© 2025 The Author(s). Steel Research International published by Wiley-VCH GmbH

1869344x, 0, Downloaded from https://onlinelibrary.wiley.com/doi/10.1002/srin.202500384 by Rwth Aachen University Zentraler Rechnungseingang, Wiley Online Library on [22/07/2025]. See the Terms and Conditions (https://onlinelibrary.wiley.com/terms-and-conditions) on Wiley Online Library for rules of use; OA articles are governed by the applicable Creative Commons License

[4] BMBF, H2Giga: Serienfertigung, https://www.wasserstoff-leitprojekte.de/leitprojekte/h2giga (accessed: October 2022).
[5] DECHEMA, ReNaRe Recycling – Nachhaltige Ressourcennutzung, https://dechema.de/Forschung/Projekte/ReNaRe.html (accessed: May 2023).
[6] S. E. Wolf, F. E. Winterhalder, V. Vibhu, L. G. J. De Haart, O. Guillon, R.-A. Eichel, N. H. Menzler, *J. Mater. Chem. A* **2023**, *11*, 17977.
[7] F. Kunz, R. Peters, D. Schäfer, S. Zhang, N. Kruse, L. G. J. De Haart, V. Vibhu, R.-A. Eichel, N. H. Menzler, C. Lenser, D. Naumenko, T. Kadyk, N. Margaritis, S. Gross-Barsnick, *ECS Trans.* **2023**, *111*, 1667.
[8] L. Blum, P. Batfalsky, Q. Fang, L. G. J. de Haart, J. Malzbender, N. Margaritis, N. H. Menzler, R. Peters, *J. Electrochem. Soc.* **2015**, *162*, F1199.
[9] S. Sarner, N. H. Menzler, A. Hilgers, O. Guillon, *ECS Trans.* **2023**, *111*, 1369.
[10] G. T. Yenesew, E. Quarez, A. L. G. L. SALLE, C. Nicollet, O. Joubert, *Resour., Conserv. Recycl.* **2023**, *190*, 106809.
[11] C. Kaiser, T. Buchwald, U. A. Peuker, *Green Chem.* **2024**, *26*, 960.
[12] S. Ahn, S. Patil, M. Rudolph, *Ind. Chem. Mater.* **2024**, *2*, 469.
[13] S. Saffirio, S. Anelli, S. Pylypko, M. K. Rath, F. Smeacetto, S. Fiorilli, *Ceram. Int.* **2024**, *50*, 34472.
[14] S. Harboe, A. Schreiber, N. Margaritis, L. Blum, O. Guillon, N. H. Menzler, *Int. J. Hydrogen Energy* **2020**, *45*, 8015.
[15] E. Hwang, C. Baek, D.-H. Peck, K. Roh, S.-Y. Yoon, S. Kang, *J. Environ. Chem. Eng.* **2025**, *13*, 115235.
[16] B. Björkman, C. Samuelsson, in *Handbook of Recycling* (Eds: E. Worrell, M.A. Reuter), Elsevier, Boston, USA **2014**, pp. 65–83.
[17] M. Chen, X. Ma, B. Chen, R. Arsenault, P. Karlson, N. Simon, Y. Wang, *Joule* **2019**, *3*, 2622.
[18] S. Manikandan, D. Inbakandan, C. Valli Nachiyar, S. Karthick Raja Namasivayam, *Sustainable Chem. Environ.* **2023**, *2*, 100001.
[19] J. Lastam, D. Sergeev, D. Grüner, M. Müller, R. Schwaiger, *Metals* **2024**, *14*, 406.
[20] S. Sarner, A. Schreiber, N. H. Menzler, O. Guillon, *Adv. Energy Mater.* **2022**, *12*, 2201805.
[21] C. Kaiser, S. Ahn, M. Brünner, D. Goes, J. Lastam, S.-O. Mongoljiibuu, S. Sarner, A. Specht, J. Fleischer, N. Menzler, M. Müller, M. Rudolph, B. Friedrich, O. Guillon, R. Schwaiger, U. Peuker, *Sustain. Mater. Technol.* **2025**, *45*, e01435.
[22] World Steel Association, World Steel in Figures **2024**, https://worldsteel.org/media/publications/ (accessed: October 2024).
[23] P. W. Griffin, G. P. Hammond, *Global Trans.* **2021**, *3*, 72.
[24] C. Harpprecht, T. Naegler, B. Steubing, A. Tukker, S. Simon, *J. Cleaner Prod.* **2022**, *380*, 134846.
[25] IEA, Iron and Steel Technology Roadmap, https://www.iea.org/reports/iron-and-steel-technology-roadmap (accessed: February 2025).
[26] Stainless Steel World Publisher, Stainless steel production 58.4 MMT in **2023**, https://stainless-steel-world.net/stainless-steel-production-58-4-mmt-in-2023/ (accessed: February 2025).
[27] World Steel Association, Stainless Steel in Figures **2022**, https://worldsteel.org/media/publications/ (accessed: September 2023).
[28] IMOA, *Practical Guidelines for the Fabrication of Austenitic Stainless Steel*, International Molybdenum Association, London, UK **2020**.
[29] T. A. Engh, G. K. Sigworth, A. Kvithyld, *Principles of Metal Refining and Recycling*, Oxford University Press, New York, USA **2021**, pp. 567–573.
[30] K. Nakajima, O. Takeda, T. Miki, K. Matsubae, T. Nagasaka, *Environ. Sci. Technol.* **2011**, *45*, 4929.
[31] M. Reuter, Y. Xiao, in *Proc. of the 35. Metallurgischen Seminar der Fachausschusses für Metallurgische Aus-und Weiterbildung der GDMB*, Aachen **1999**, pp. 95–140.
[32] Y. Xiao, L. Holappa, *Thermodynamic Properties of Chromium Bearing Slags and Minerals*, Helsinki University of Technology, Espoo **1996**, pp. 39–42.
[33] R. L. Klueh, P. J. Maziasz, E. H. Lee, *Mater. Sci. Eng.: A* **1988**, *102*, 115.
[34] A. Weiss, H. Gutte, M. Radtke, P. Scheller, US 2009/0324441 A, **2009**.
[35] A. Almomani, A.-H. I. Mourad, I. Barsoum, *Eng. Failure Anal.* **2022**, *139*, 106488.
[36] F. Gauzzi, R. Montanari, G. Principi, M. E. Tata, *Mater. Sci. Eng.: A* **2006**, *438–440*, 202.
[37] M. J. Sohrabi, M. Naghizadeh, H. Mirzadeh, *Archiv. Civ. Mech. Eng* **2020**, *20*, 124.
[38] M. F. McGuire, *Stainless Steels for Design Engineers*, ASM International, Ohio, USA **2008**, pp. 161–171.
[39] D. Schäfer, Q. Fang, L. Blum, D. Stolten, *J. Power Sources* **2019**, *433*, 126666.
[40] M. Moallemi, A. Zarei-Hanzaki, M. Eskandari, A. Burrows, H. Alimadadi, *Metall. Mater. Trans. A* **2017**, *48*, 3675.
[41] M. Buchmann, N. Borowski, T. Leißner, T. Heinig, M. A. Reuter, B. Friedrich, U. A. Peuker, *Minerals* **2020**, *10*, 309.
[42] S. Hampel, I. A. Alhafez, A. Schnickmann, S. Wunderlich, H. Li, M. Fischlschweiger, T. Schirmer, N. Merkert, U. E. A. Fittschen, *Minerals* **2024**, *14*, 868.
[43] FactSage, What's New in FactSage 8.3, https://www.factsage.com/facthelp/FS83 New.htm. (accessed: January 2025).
[44] SGTE, SGTE Solution Database (SGSOL), https://www.sgte.net/en/sgte-solution-database-sgsol (accessed: January 2025).
[45] H. R. Brager, F. A. Garner, *J. Nuclear Mater.* **1978**, *73*, 9.
[46] S. M. Levine, C. Pareige, Z. Jiao, P. D. Edmondson, G. S. Was, S. J. Zinkle, A. Bhattacharya, *Mater. Des.* **2022**, *217*, 110588.
[47] D. Y. Liu, M. J. Zhao, N. R. Tao, *Scr. Mater.* **2023**, *230*, 115396.
[48] G. F. V. Voort, in *Analytical Characterization of Aluminum, Steel, and Superalloys* (Eds: D. S. MacKenzie, G. E. Totten), CRC Press, Boca Raton, USA **2005**, p. 78.
[49] K. Sangwal, B. Surowska, P. Błaziak, *Mater. Chem. Phys.* **2003**, *77*, 511.
[50] J. Mola, E. J. Seo, L. Cho, *Mater. Sci. Eng.: A* **2021**, *822*, 141687.
[51] L. Xiao, Z. Fan, Z. Jinxiu, Z. Mingxing, K. Mokuang, G. Zhenqi, *Phys. Rev. B* **1995**, *52*, 9970.
[52] Euro Inox, *Stainless Steel: Tables of Technical Properties*, Vol. *5*, Euro Inox, Luxembourg, Luxembourg **2007**.
[53] G. Ghosh, G. B. Olson, *Acta Metall. Mater.* **1994**, *42*, 3361.
[54] Q. X. Dai, X. N. Cheng, Y. T. Zhao, X. M. Luo, Z. Z. Yuan, *Mater. Charact.* **2004**, *52*, 349.
[55] S. S. F. D. Dafé, F. L. Sicupira, F. C. S. Matos, N. S. Cruz, D. R. Moreira, D. B. Santos, *Mat. Res.* **2013**, *16*, 1229.
[56] S. M. C. van Bohemen, L. Morsdorf, *Acta Mater.* **2017**, *125*, 401.
[57] Q. Gao, C. Wang, F. Qu, Y. Wang, Z. Qiao, *J. Alloys Compd.* **2014**, *610*, 322.
[58] A. Gramlich, T. Hinrichs, H. Springer, U. Krupp, *Steel Res. Int.* **2023**, *94*, 2200623.
[59] J. Liu, J. Sun, S. Wei, S. Lu, *Crystals* **2021**, *11*, 709.
[60] A. Baghdadchi, V. A. Hosseini, L. Karlsson, *J. Mater. Res. Technol.* **2021**, *15*, 3610.
[61] S. H. Kim, H. K. Moon, T. Kang, C. S. Lee, *Mater. Sci. Eng.: A* **2003**, *356*, 390.
[62] V. S. Raghunathan, V. Seetharaman, S. Venkadesan, P. Rodriguez, *Metall. Trans. A* **1979**, *10*, 1683.
[63] F. S. Shieu, Y. C. Sung, L. H. Cheng, J. H. Huang, G. P. Yu, *Corros. Sci.* **1997**, *39*, 893.
[64] P. Niranatlumpong, H. Koiprasert, *Surf. Coat. Technol.* **2006**, *201*, 737.
[65] X. Wang, J. J. Noël, I. O. Wallinder, Y. S. Hedberg, *Mater. Des.* **2021**, *198*, 109393.
[66] G. Eichenbaum, J. T. Wilsey, G. Fessel, Q.-Q. Qiu, L. Perkins, P. Hasgall, A. Monnot, S. L. More, N. Egnot, J. Sague, S. Marcello, K. Connor, J. Scutti, W. V. Christian, P. M. Coplan, J. Wright, B. Hastings, L. B. Katz, M. Vreeke, M. Calistri-Yeh, B. Faiola,

© 2025 The Author(s). Steel Research International published by Wiley-VCH GmbH

1869344x, 0, Downloaded from https://onlinelibrary.wiley.com/doi/10.1002/srin.202500384 by Rwth Aachen University Zentraler Rechnungseingang, Wiley Online Library on [22/07/2025]. See the Terms and Conditions (https://onlinelibrary.wiley.com/terms-and-conditions) on Wiley Online Library for rules of use; OA articles are governed by the applicable Creative Commons License

B. Purushothaman, J. Nevelos, M. Bashiri, J. B. Christensen, M. Kovochich, K. Unice, *Regul. Toxicol. Pharmacol.* **2021**, *125*, 105004.
[67] A. J. Niri, G. A. Poelzer, S. E. Zhang, J. Rosenkranz, M. Pettersson, Y. Ghorbani, *Renewable Sustainable Energy Rev.* **2024**, *191*, 114176.
[68] E. Commission, E. Directorate-General for Internal Market IndustrySMEs, M. Grohol, C. Veeh, *Study on The Critical Raw Materials for the EU 2023 – Final Report*, Publications Office of the European Union, Luxembourg, Luxembourg **2023**.
[69] J. C. Koj, P. Zapp, C. Wieland, K. Görner, W. Kuckshinrichs, *Energ Sustainable Soc.* **2024**, *14*, 64.
[70] C. Davis, R. Hall, S. Hazra, K. Debattista, S. Zhuang, J. Duan, Z. Li, J. Shenton, D. Panni, A. Halfpenny, *Phil. Trans. R. Soc. A.* **2024**, *382*, 20230244.
[71] S. Bai, S. Zhang, J. Ma, J. Li, L. Mou, *J. Mater. Res. Technol.* **2024**, *30*, 4750.
[72] C. Pascal, V. Parry, E. Fedorova, M. Braccini, P. Chemelle, N. Meyer, D. Oquab, D. Monceau, Y. Wouters, M. Mantel, *Corros. Sci.* **2015**, *93*, 100.
[73] B. Padmanabhan, P. Salunkhe, D. Nage, *J. Failure Anal. Prev.* **2015**, *15*, 480.
[74] S. Rao, A. Y. Al-Kawaie, *Weld. J.* **2010**, *89*, 46.
[75] E. Matinde, J. Steenkam, in *Metallurgical Slags: Environmental Geochemistry and Resource Potential* (Eds: N. Piatak, V. Ettler), The Royal Society of Chemistry, Croydon, UK **2021**, pp. 14–58.
[76] C. Rachmawati, J. Weiss, H. I. Lucas, E. Löwer, T. Leißner, D. Ebert, R. Möckel, B. Friedrich, U. A. Peuker, *Minerals* **2024**, *14*, 130.
[77] T. T. Võ, T. Leißner, U. A. Peuker, *Minerals* **2024**, *14*, 42.
[78] VDM Metals, *VDM Metals International GmbH*, Werdohl, Germany **2022**.

© 2025 The Author(s). Steel Research International published by Wiley-VCH GmbH

1869344x, 0, Downloaded from https://onlinelibrary.wiley.com/doi/10.1002/srin.202500384 by Rwth Aachen University Zentraler Rechnungseingang, Wiley Online Library on [22/07/2025]. See the Terms and Conditions (https://onlinelibrary.wiley.com/terms-and-conditions) on Wiley Online Library for rules of use; OA articles are governed by the applicable Creative Commons License